sustainability

MDPI

Article

Sustainability-Oriented Parametric Exergetic Analysis of Liquid Air Energy Storage Systems with Waste Heat and Cold Recovery

Adalia Andreea Percembli (Chelmuș) [1,*], Lavinia Grosu [2], Dănuț Cristian Urduza [1] and Alexandru Dobrovicescu [1,*]

[1] Department of Engineering Thermodynamics, National University of Science and Technology Politehnica Bucharest, 060042 Bucharest, Romania; danut.urduza@stud.mec.upb.ro
[2] Laboratoire Energétique Mécanique Electromagnétisme (LEME), IUT de Ville d'Avray, 50 Rue de Sèvres, 92410 Ville d'Avray, France; mgrosu@parisnanterre.fr
* Correspondence: adalia.chelmus@stud.mec.upb.ro (A.A.P.); adobrovicescu@upb.ro (A.D.)

Abstract

Liquid Air Energy Storage (LAES) is a promising large-scale storage technology for supporting the sustainable integration of intermittent renewable electricity into power grids, particularly when electricity storage is combined with waste-heat valorization, cryogenic cold recovery, and reduced exergy degradation. In this thermodynamic sense, the present study proposes a sustainability-oriented framework for the comparative and parametric exergetic analysis of LAES systems, integrating the liquefaction and discharge stages within a unified analysis. The assessment focuses on thermodynamic resource efficiency and exergy performance rather than on a complete economic, environmental, or life-cycle evaluation. The objective is to identify the components and operating parameters that most strongly influence performance and to quantify the reductions in exergy destruction and losses achieved through configuration changes and parameter variation. Three Linde–Hampson-based liquefaction configurations are compared, including arrangements with external and intermediate auxiliary pre-cooling. Improved heat-exchanger integration and temperature matching increase the structural liquefaction exergetic indicator from 7.95% in the baseline configuration to 19.28% in the two-RHX configuration. The discharge stage is assessed parametrically with respect to cryogenic pumping pressure, turbine inlet temperature, and expansion architecture. Single-stage and two-stage adiabatic expansions are compared with an ideal isothermal benchmark. The adiabatic configurations provide mechanical-work recovery together with recoverable cooling potential, whereas the isothermal case gives the highest work-recovery benchmark. Under the reference conditions, using the aggregated compressor representation adopted for the main parametric analysis, the two-stage adiabatic configuration reaches a global exergetic efficiency of 15.92% for the improved Linde–Hampson-based chain and 24.87% for the selected Claude–Heylandt reference block.

Keywords: liquid air energy storage; sustainable energy storage; parametric exergy analysis; renewable energy integration; Linde–Hampson cycle; Claude–Heylandt cycle; global exergetic efficiency; cryogenic energy storage; waste-heat recovery

Check for updates

Academic Editor: John Bell

Received: 5 June 2026
Revised: 11 August 2026
Accepted: 17 August 2026
Published: 21 August 2026

Copyright: © 2026 by the authors. Licensee MDPI, Basel, Switzerland. This article is an open access article distributed under the terms and conditions of the Creative Commons Attribution (CC BY) license.

1. Introduction

The transition toward low-carbon energy systems requires the large-scale integration of variable renewable sources, such as wind and solar energy. Their variability increases mismatches between generation and demand, creates periods of surplus production, and

intensifies the need for balancing resources, making energy storage an essential component of sustainable energy infrastructure [1,2]. In this context, storage systems must be analyzed not only as accumulation solutions, but also as subsystems integrated with the grid, with available heat and cold sources, and with energy recovery requirements [1–3].

Among large-capacity storage solutions, Liquid Air Energy Storage (LAES) is of particular interest because of its high storage density, the use of atmospheric air as the working fluid, and its relative independence from geographical or geological constraints. LAES provides siting flexibility and can be integrated with industrial waste-heat sources, thermal networks, or applications that use the cooling generated during the discharge stage [4–7]. Therefore, LAES can support sustainable energy infrastructures, especially when electricity storage is integrated with waste-heat utilization and recoverable cooling potential.

A LAES system operates through two main stages: during the charge stage, air is compressed, cooled, liquefied, and stored in a cryogenic tank; during discharge, liquid air (LA) is pumped, regasified, heated, and expanded in a turbine to produce mechanical work. Depending on the architecture, useful secondary products can also be obtained, such as recoverable cooling or chilled water [5,6].

From a sustainability perspective, LAES performance cannot be evaluated only on an energy basis because irreversibilities reduce the ability of energy to produce useful work. Exergy analysis is therefore required to identify exergy losses and opportunities for improvement, and the reduction in exergy destruction becomes an important criterion for sustainable design. Within a broader sustainability assessment, these thermodynamic indicators represent only part of a complete 4E framework, which may also include economic and environmental criteria. The present study focuses on the energy and exergy dimensions of LAES performance, providing a thermodynamic basis for subsequent techno-economic, environmental, or life-cycle assessments.

The recent literature has addressed LAES in terms of system configuration, thermal integration, and global performance. Borri et al. [4] and Vecchi et al. [5] highlighted the role of hybrid solutions and the recovery of compression heat and cryogenic cold energy, while She et al. [7] and Qi et al. [6] emphasized the challenges associated with the efficient production of liquid air and its use as an energy vector for power and cooling. Other studies have investigated the integration of LAES with heat and cold sources: Peng et al. [8] showed the importance of cold recovery, Tafone et al. [9] proposed integration with an ORC and an absorption chiller, Vecchi et al. [10] analyzed the use of LAES in thermal networks, and Liu et al. [11] and Peng et al. [12] investigated thermal energy recovery and the use of external cold energy from liquefied natural gas (LNG) regasification, respectively. These contributions confirm the value of thermal integration for increasing resource efficiency, but the improvements are often achieved by adding or optimizing auxiliary subsystems.

Liquefaction technology remains a critical factor for the global performance and sustainability of LAES systems. Dzido et al. [13] and Kiliç and Altun [14] showed that the choice of liquefaction cycle decisively influences energy consumption, efficiency, and operating parameters. An energy and exergy analysis of the simple Linde–Hampson cycle identified the warm-end temperature difference and compression pressure as key decision parameters and examined their effects on liquid yield, specific work consumption, COP, and the principal exergy-destruction contributions [15]. A structural analysis by Urduza et al. [16] further reported that throttling and compression contributed approximately 41% and 40%, respectively, to total exergy destruction, followed by heat transfer across a finite temperature difference in the recuperative heat exchanger. Throttling fragmentation, Reverse Pinch analysis, and optimization of mass-flow-rate ratios reduced irreversibilities and improved thermal and hydraulic coupling. For the Claude–Heylandt cycle, Urduza et al. [17] showed that the introduction of an expander in parallel with the throttling valve

and optimization of the thermal profile can reduce the exergy destruction associated with heat transfer from 14% to 3.5%. In LAES applications, Szablowski et al. [18] identified the air evaporator and the Joule–Thomson valve as critical zones, while Manesh and Ghorbani [19] demonstrated the potential of hybridization, although with increased structural complexity.

A research direction closer to the objective of this work is advanced exergy analysis, in which exergy destruction is divided into avoidable/unavoidable and endogenous/exogenous components. Incer-Valverde et al. [20] applied this method to a large-scale cryogenics-based energy storage system, while Bucsa et al. [21], Hamayun et al. [22], and Percembli et al. [23] highlighted the role of compression, heat exchange, and equipment configuration in cryogenic air separation systems. However, these studies mainly focus on component assessment or the optimization of given configurations, rather than on the structural interpretation of the exergy balance for an inverse liquefaction cycle. In such a system, the balance terms should not be interpreted indiscriminately as losses or destruction: some contributions can be reduced by design, some are partially recoverable, and others represent minimum consumptions imposed by the cycle architecture and by the state of the cryogenic product.

In the present work, concepts from advanced exergy analysis are used only as a methodological reference. The proposed approach is a structural product–fuel interpretation of the liquefaction balance, aimed at separating the useful cryogenic product, reducible irreversibilities and losses, and the minimum thermodynamic consumption imposed by the selected liquefaction scheme.

From a sustainability perspective, LAES should not be assessed solely as an electricity-storage technology but also as a multi-energy system capable of improving resource efficiency in low-carbon energy networks. By storing surplus renewable electricity, LAES can contribute to reducing renewable curtailment, enhancing grid flexibility, and supporting the decarbonization of electricity supply. During discharge, available industrial waste heat can be valorized to enhance mechanical-work recovery, while chilled water and the cold turbine exhaust may provide recoverable cooling potential when suitable external sinks are available. This integration can improve the use of otherwise rejected thermal resources and, where the cooling potential is effectively utilized, may reduce the demand placed on separate refrigeration systems. These potential benefits depend strongly on the thermodynamic performance of the liquefaction and recovery processes. Accordingly, within the present thermodynamic scope, reducible exergy destruction and exergy losses are used as indicators of resource degradation, while external-heat utilization, mechanical-work recovery, and recoverable cooling potential characterize resource recovery.

This paper proposes a physically interpretable exergetic framework for the analysis of a LAES system based on inverse cryogenic cycles, with emphasis on the structural reinterpretation of the exergy balance of the liquefaction process. The exergy of states that are simultaneously in thermal and mechanical disequilibrium with the ambient environment is decomposed into thermal and mechanical components through physically interpretable reversible paths. This approach allows the recoverable cooling potential to be separated from scheme-imposed minimum thermodynamic consumptions, from recoverable or unrecoverable losses, and from exergy destruction that can be reduced through configuration and operating-parameter changes. In this way, the exergy balance becomes a structural diagnostic tool for sustainable system design, for resource-efficient liquefaction, and for improved mechanical-work recovery and recoverable cooling potential.

The novelty of the present contribution should therefore be understood at the LAES-system level rather than at the level of proposing a new elementary Linde–Hampson or Claude–Heylandt liquefaction cycle. Compared with previous cycle-level studies, the present work embeds the structurally interpreted liquefaction balance into a complete

LAES chain, in which the exergetic product of liquefaction is transferred internally from the liquefaction block to the discharge stage and is then evaluated together with the utilization of an available external thermal stream, mechanical-work recovery, and the cooling potential that may be recovered when a suitable external sink is available. This common product–fuel interpretation allows the influence of liquefaction technology on the global exergetic performance of the modeled liquefaction–recovery chain to be assessed without changing the discharge-stage assumptions. The comparison is developed through controlled configuration changes and one-factor parametric analyses under a common set of assumptions, so that the thermodynamic effect of each structural or operating decision remains visible.

On this basis, three Linde–Hampson configurations are analyzed: the basic cycle with single throttling, the cycle with external auxiliary pre-cooling, and the modified cycle with two recuperative heat exchangers and intermediate auxiliary pre-cooling. The discharge stage is then investigated through the cryogenic pumping pressure, the turbine inlet temperature, and three expansion architectures: single-stage adiabatic expansion, two-stage adiabatic expansion with reheating, and ideal isothermal expansion as an upper thermodynamic benchmark. The useful output is treated as a multi-energy product comprising mechanical work and recoverable cooling potential, while the comparison with the selected Claude–Heylandt reference architecture highlights the strong influence of liquefaction technology on the global exergetic efficiency and thermodynamic resource efficiency of the modeled LAES chain.

2. Basic Linde–Hampson Cycle with Storage Pressure Above Ambient Pressure

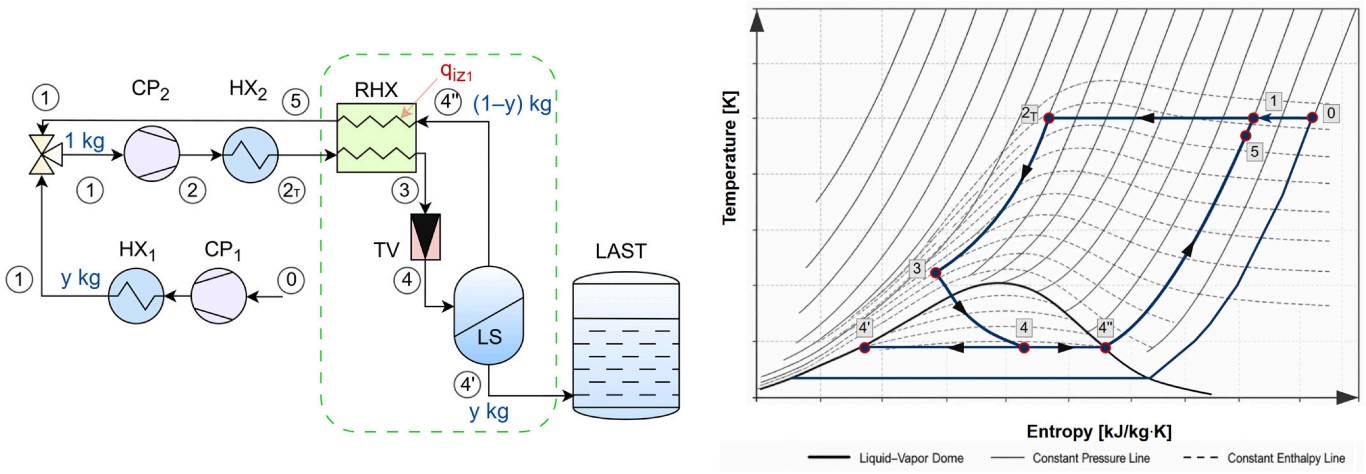
For the analysis of cryogenic energy storage systems, the classical Linde–Hampson cycle is a fundamental starting point because it describes the basic mechanism of gas liquefaction by successive compression and expansion. The process uses the Joule–Thomson effect of real gases, through which isenthalpic expansion produces a temperature drop, facilitating the conditions required for transition to the liquid phase.

2.1. Schematic Configuration of the Single-Stage Throttling Process

The conceptual scheme and the representation of the classical Linde–Hampson cycle in the T–s diagram are shown in Figure 1. The sequence of processes is as follows: compression of make-up air (0–1) and of the total air flow rate (1–2_T), cooling of the compressed air (CA) stream (2_T–3) by regenerative heating of the cold gas (4″–5), throttling of the compressed air stream (3–4), and separation of liquid air (4′) from the gaseous fraction (4″).

For process modeling, a unit mass basis is adopted, with 1 kg of air entering the main compressor CP_2 at state 1. After theoretical compression and cooling to ambient conditions (1–2_T), the high-pressure gas stream is pre-cooled in the recuperative heat exchanger RHX (2_T–3) through heat transfer with the return gas stream (4″–5). Isenthalpic expansion (3–4) in the throttling valve (TV) produces a two-phase mixture, which is introduced into the liquid separator (LS). The liquid fraction (state 4′) is directed to the liquid air storage tank (LAST), while the gaseous fraction (state 4″) is recirculated through the recuperative heat exchanger, providing cooling for the high-pressure stream. Because of the elevated storage pressure in LAST, an auxiliary compression stage (CP_1), together with intermediate cooling (HX_1), is required to raise the make-up air to the main-cycle inlet pressure, thereby maintaining the unit flow rate of the cycle. At the outlet of RHX, the low-pressure air stream is heated in the compressor suction line (5–1).

https://doi.org/10.3390/su18168605



(**a**) (**b**)

Figure 1. Linde–Hampson air liquefaction system: (**a**) system layout; (**b**) schematic T–s diagram of the cycle (not to scale).

2.2. Mathematical Modeling

The energy and exergy analyses of the system were performed using the Engineering Equation Solver (EES) computational environment [24], which includes a thermodynamic property library for evaluating the real-fluid properties of the working fluid. Air properties were evaluated using the EES fluid AIR_ha, which represents standard dry air as a fixed-composition real-fluid mixture based on the fundamental equation of state of Lemmon et al. [25]. The adopted molar composition is $x_{N_2} = 0.7812$, $x_{O_2} = 0.2096$, and $x_{Ar} = 0.0092$; carbon dioxide and water vapor are not included. The correlation is applicable from 60 to 2000 K and at pressures up to 2000 MPa, covering the thermodynamic range considered in this study. Gas, liquid, saturated, and two-phase properties are evaluated using the same fixed-composition AIR_ha formulation.

After defining the common real-fluid property formulation, the liquefaction blocks and the recovery-stage turbine model were compared with the literature data to assess consistency in trends and orders of magnitude. Supplementary Table S6 reports the corresponding differences for liquid yield, specific liquefaction work, COP or exergetic indicator, gross turbine work, and net recovery work. Only the near-matched recovery-turbine case is used as a quantitative check; the liquefaction comparisons involve different assumptions, topologies, or system boundaries and are used only as supporting consistency comparisons.

The calculations are formulated as a steady-state comparative model. The same reference environment, AIR_ha property formulation, mass basis, and product–fuel definitions are applied to all configurations. Distributed pressure drops in the recuperators, heaters, connecting lines, valves, storage connections, and discharge train are not modeled; the reported differences therefore represent idealized thermodynamic upper-bound comparisons rather than equipment-level design values. One-factor sensitivities to heat ingress, recuperator temperature approach, compressor efficiency, and auxiliary refrigeration COP are reported in Supplementary Table S7, while Supplementary Table S8 presents combined deterministic bounding cases. These analyses do not constitute probabilistic uncertainty propagation or confidence intervals.

Thermal feasibility was checked by segmented temperature–enthalpy analysis for the baseline RHX, the external pre-cooling RHX, RHX_1, RHX_2, HX_3, and HX_4. At each operating point, each exchanger was divided into 100 equal intervals of air-stream enthalpy, corresponding to 101 calculation nodes, and the minimum local temperature difference

and its position were recorded. The verification covered the complete investigated ranges of p_1, p_2, T_6, T_7, p_9, and T_{11}; the results are reported in Supplementary Table S9.

2.2.1. Energy Analysis

For the configuration in Figure 1, the liquefied air fraction is determined by applying the energy balance to the green control boundary that includes RHX, TV, and LS. In this case, state 1 represents the gas state at the inlet of the main compressor, at the operating pressure p_1, with $p_1 > p_0$, while state 0 is the reference state of the gas taken from the ambient environment before preliminary compression. The main design parameters considered are the storage pressure p_1 and the upper compression pressure p_2.

For 1 kg of gas entering the recuperative heat exchanger at state 2_T, throttling and separation produce y kg of liquid at state $4'$ and $(1 - y)$ kg of recirculated saturated vapor, which leaves RHX at state 5. Taking heat ingress through insulation into account, the energy balance applied to the green boundary in Figure 1a gives the liquid air fraction as

$$y = \frac{h_5 - h_{2_T} - q_{iz}}{h_5 - h_{4'}}. \quad (1)$$

If the enthalpy variation along the isotherm T_1, between pressures p_1 and p_2, associated with the Linde–Hampson cooling effect, is quantified by

$$\left|\Delta h_{T,1-2_T}\right| = h_1 - h_{2_T}, \quad (2)$$

the warm-end cooling loss in RHX, caused by the need to maintain a finite temperature difference at the warm end of the apparatus, is expressed as

$$q_n = h_1 - h_5, \quad (3)$$

and the specific cooling capacity of the gas for state 1 is expressed as

$$q_f = h_1 - h_{4'}, \quad (4)$$

then the liquefied air fraction can be rewritten as

$$y = \frac{\left|\Delta h_{T,1-2_T}\right| - q_n - q_{iz}}{q_f - q_n}. \quad (5)$$

The mechanical work supplied to the system is divided between two compression processes. The main compressor CP_2 acts on the main circuit, while the auxiliary compressor CP_1 acts only on the make-up fraction y. Therefore, per unit mass, the mechanical work supplied to the system is

$$\left|W_{cp}\right| = \left|w_{cp,2}\right| + y\left|w_{cp,1}\right|, \quad (6)$$

where

$$\left|w_{cp,2}\right| = \frac{\left|w_{cp,T_0}^{1-2_T}\right|}{\eta_{cp,T}}, \text{ and } \left|w_{cp,1}\right| = \frac{\left|w_{cp,T_0}^{0-1}\right|}{\eta_{cp,T}}, \quad (7)$$

with the reversible isothermal terms evaluated using real-gas properties in EES.

The coefficient of performance (COP) of the real cycle is

$$COP = \frac{Q_f}{\left|w_{cp,2}\right| + y\left|w_{cp,1}\right|} = \frac{y(q_f - q_n)}{\left|w_{cp,2}\right| + y\left|w_{cp,1}\right|}. \quad (8)$$

To obtain 1 kg of liquefied air, the specific energy consumption is calculated as follows:

$$w_0 = \frac{|w_{cp}|}{y} = \frac{|w_{cp,2}| + y|w_{cp,1}|}{y} = \frac{|w_{cp,2}|}{y} + |w_{cp,1}|. \quad (9)$$

2.2.2. Exergy Analysis

Unlike energy, exergy is not conserved but is consumed in irreversible processes. Consequently, the exergy balance for a control volume is written as

$$\sum Ex_i = \sum Ex_e + \sum I, \quad (10)$$

where Ex represents the exergy of a fluid stream, subscripts i and e correspond to inlet and outlet states, respectively, and I represents exergy destruction due to irreversibilities.

Applying the exergy balance given by Equation (10) to the green dashed boundary in Figure 1a can be written as

$$Ex_{2_T} + Ex_{Q_{iz}} = Ex_{4'} + Ex_5 + i_{JT} + I_{\Delta T}, \quad (11)$$

where i_{JT} is the exergy destruction associated with the Joule–Thomson (JT) effect due to throttling.

Ex_{2_T} represents the exergy of the compressed stream (with a mass of 1 kg) cooled to ambient temperature. Because state 2_T has the same temperature as the ambient environment but a higher pressure, its exergy is exclusively mechanical. It is equal to the maximum mechanical work that could be obtained by reversible isothermal expansion from pressure p_2 to p_0, at temperature T_0, or equivalently to the minimum reversible isothermal compression work from p_0 to p_2:

$$Ex_{2_T} = 1 \cdot ex_{2_T} = ex_{2_T} - ex_0 = h_{2_T} - h_0 - T_0(s_{2_T} - s_0) = \left|w_{cp,T_0}^{0-2_T}\right|. \quad (12)$$

$Ex_{Q_{iz}}$ can be interpreted as the minimum mechanical work required to remove the heat ingress through insulation from the ambient environment by means of a refrigeration machine operating according to the Carnot cycle. Thus, the exergetic penalty associated with heat ingress through the insulation of the recuperative heat exchanger is evaluated as

$$|Ex_{Q_{iz}}| = q_{iz}|\theta_{q_{iz}}| = q_{iz}\left(\frac{T_0}{T_{m_{4''-5}}} - 1\right), \quad (13)$$

where $T_{m_{4''-5}}$ is the mean thermodynamic temperature between states 4″ and 5.

The exergy of the stream at state 5 can be written in the general form

$$Ex_5 = (1 - y)ex_5 = (1 - y)[h_5 - h_0 - T_0(s_5 - s_0)]. \quad (14)$$

To highlight both the thermal and mechanical exergy of state 5, the system is considered to follow the reversible path (5–1–0) on its way to equilibrium with the ambient environment. With this convention, Equation (14) becomes

$$Ex_5 = (1 - y)\{(h_5 - h_1) + (h_1 - h_0) - T_0[(s_5 - s_1) + (s_1 - s_0)]\} = Ex_5^T + Ex_5^M. \quad (15)$$

The evolution along path (5–1) represents the thermal component Ex_5^T, while path (1–0), represents the mechanical component Ex_5^M of the exergy of state 5.

$$Ex_5^T = (1 - y)[(h_5 - h_1) - T_0(s_5 - s_1)] = (1 - y)(h_5 - h_1)\left(1 - \frac{T_0}{T_{m,5-1}}\right) \quad (16)$$

Since $q_n = h_1 - h_5$, Equation (16) becomes

$$Ex_5^T = (1-y)q_n\left(\frac{T_0}{T_{m,5-1}} - 1\right) = \left|Ex_{q_{5-1}}^{T_{m,5-1}}\right| = L_{\Delta T_n}\,, \tag{17}$$

which represents the exergy of the heat that was not extracted from the main air stream because of the need to ensure a temperature difference ΔT_n at the warm end of the recuperative heat exchanger. For the system, Ex_5^T represents an exergy loss.

The mechanical component obtained along path (1–0) can be written as the mechanical work of a reversible isothermal expansion at temperature T_0, from pressure p_1 to p_0, equal in absolute value to the isothermal compression work from p_0 to p_1:

$$Ex_5^M = (1-y)[(h_1 - h_0) - T_0(s_1 - s_0)] = (1-y)\left|w_{cp,T_0}^{0-1}\right| \tag{18}$$

The exergy of state 4′ is given by the general relation

$$Ex_{4'} = y[(h_{4'} - h_0) - T_0(s_{4'} - s_0)]. \tag{19}$$

State 4′ has thermomechanical exergy, being in both mechanical and thermal disequilibrium with the ambient environment (p_0, T_0). To reach thermomechanical equilibrium with the ambient environment, the system may follow the reversible path (4′–1–0). Thus, Equation (19) can be written as

$$Ex_{4'} = y\{(h_{4'} - h_1) + (h_1 - h_0) - T_0[(s_{4'} - s_1) + (s_1 - s_0)]\} = Ex_{4'}^T + Ex_{4'}^M \tag{20}$$

The thermal component of the exergy of state 4′ is

$$Ex_{4'}^T = y[(h_{4'} - h_1) - T_0(s_{4'} - s_1)] = y(h_{4'} - h_1)\left(1 - \frac{T_0}{T_{m,4'-1}}\right) \tag{21}$$

Noting that $|q_f| = h_1 - h_{4'} > 0$ and that the exergetic factor $\left|\theta_{q_f}\right| = \left(\frac{T_0}{T_{m,4'-1}} - 1\right) > 0$, Equation (21) becomes

$$Ex_{4'}^T = y|q_f| \cdot \left|\theta_{q_f}\right| = \left|Ex_{Q_f}\right| \tag{22}$$

and represents the thermal component of the useful cryogenic product.

The mechanical component of the exergy of state 4′ is the mechanical work produced by the fraction y in an isothermal expansion process from p_1 to p_0, equal in absolute value to the isothermal compression work from p_0 to p_1:

$$Ex_{4'}^M = y[(h_1 - h_0) - T_0(s_1 - s_0)] = y\left|w_{cp,T_0}^{0-1}\right|. \tag{23}$$

By substituting the expressions obtained for Ex_{2_T}, $Ex_{4'}$, Ex_5, and $Ex_{Q_{iz}}$ into balance (11), a relation is obtained in which the product, exergy losses, and exergy destruction can be identified:

$$\left|w_{cp,T_0}^{0-2_T}\right| = L_{Q_{iz}} + \left|Ex_{Q_f}\right| + y\left|w_{cp,T_0}^{0-1}\right| + L_{\Delta T_n} + (1-y)\left|w_{cp,T_0}^{0-1}\right| + i_{JT} + I_{\Delta T} \tag{24}$$

where $L_{Q_{iz}}$ represents the exergy loss associated with heat ingress through insulation, $L_{\Delta T_n}$ represents the exergy loss associated with the impossibility of fully recovering the cold potential of the cold stream at the warm end of the heat exchanger, and $I_{\Delta T}$ is the exergy destruction associated with heat transfer across a finite temperature difference.

Equation (24) can be reorganized by moving the mechanical term of the $(1-y)$ stream to the left-hand side

$$\left|w_{cp,T_0}^{0-2_T}\right| - (1-y)\left|w_{cp,T_0}^{0-1}\right| = \left|Ex_{Q_f}\right| + y\left|w_{cp,T_0}^{0-1}\right| + i_{JT} + I_{\Delta T} + L_{\Delta T_n} + L_{Q_{iz}} \tag{25}$$

where the exergy destruction due to throttling is

$$i_{JT} = T_0(s_4 - s_3), \tag{26}$$

and the exergy destruction due to heat transfer across a finite temperature difference is

$$I_{\Delta T} = T_0\left[(1-y)s_5 + s_3 - s_{2_T} - (1-y)s_{4''}\right] \tag{27}$$

The left-hand side of Equation (25) contains what the system consumes, while the right-hand side contains what it should consume at minimum, supplemented by exergy consumptions (destruction) and losses.

Considering the isothermal efficiency of compression, the real mechanical-work consumption is obtained:

$$\left|W_{cp}\right| = \frac{\left|w_{cp,T_0}^{1-2_T}\right| + y\left|w_{cp,T_0}^{0-1}\right|}{\eta_{cp,T}}. \tag{28}$$

where the reversible isothermal terms, evaluated using real-gas properties in EES, are given by

$$\left|w_{cp,T_0}^{1-2_T}\right| = h_{2_T} - h_1 - T_0(s_{2_T} - s_1), \text{and } \left|w_{cp,T_0}^{0-1}\right| = h_1 - h_0 - T_0(s_1 - s_0). \tag{29}$$

The compression model represents each compressor and its associated cooling process as an aggregate compressor–cooler, with the compressed air returned to T_0. For this control boundary, the excess mechanical input relative to reversible isothermal compression is distributed between internal exergy destruction and the physical exergy rejected with the cooling heat:

$$I_{cp,2} + \left|Ex_{Qcp_2}\right| = \left|w_{cp,T_0}^{1-2_T}\right|\left(\frac{1}{\eta_{cp,T}} - 1\right) \text{ and } I_{cp,1} + \left|Ex_{Qcp_1}\right| = y\left|w_{cp,T_0}^{0-1}\right|\left(\frac{1}{\eta_{cp,T}} - 1\right). \tag{30}$$

Accounting for Equations (28) and (30), Equation (24) gives

$$\left|W_{cp}\right| = \left|Ex_{Q_f}\right| + y\left|w_{cp,T_0}^{0-1}\right| + i_{JT} + I_{\Delta T} + I_{cp,2} + \left|Ex_{Qcp_2}\right| + I_{cp,1} + \left|Ex_{Qcp_1}\right| + L_{\Delta T_n} + L_{Q_{iz}}. \tag{31}$$

The term $y\left|w_{cp,T_0}^{0-1}\right|$ represents the minimum reversible compression work required to bring the liquefied fraction from the ambient pressure p_0 to the storage pressure p_1. This contribution is not an exergy-destruction term in the conventional Gouy–Stodola sense and is not intended to represent the unavoidable part of a formal advanced exergy decomposition. It is instead a scheme-imposed minimum thermodynamic consumption associated with delivering the useful cryogenic product at the selected storage pressure:

$$C_{min}^{sch} = y\left|w_{cp,T_0}^{0-1}\right| \tag{32}$$

With these considerations, Equation (31) can be written as

$$\left|W_{cp}\right| = \left|Ex_{Q_f}\right| + C_{min}^{sch} + \sum I_i + \sum L_i, \tag{33}$$

where C_{min}^{sch} is the scheme-imposed minimum thermodynamic consumption,

$$\sum I_i = i_{JT} + I_{\Delta T} + I_{cp,2} + I_{cp,1} \text{ and} \tag{34}$$

$$\sum L_i = L_{\Delta T_n} + L_{Q_{iz}} + \left|Ex_{Qcp_1}\right| + \left|Ex_{Qcp_2}\right|. \tag{35}$$

Within this extended balance, C_{min}^{sch} is retained separately from exergy destruction (I_i) and losses (L_i) because it is imposed by the selected cycle architecture and storage

pressure rather than generated by internal irreversibility. The resulting classification is therefore used as a structural product–fuel interpretation of the cycle balance.

The terms i_{JT}, $\dot{I}_{\Delta T}$, $L_{\Delta T_n}$, $L_{Q_{iz}}$ and I_{cp}, can be reduced through constructive or operational measures, while C_{min}^{sch} is the minimum consumption imposed by the selected scheme.

To characterize the conversion of the mechanical input into the thermal component of the cryogenic product, the structural liquefaction exergetic indicator is defined as

$$\eta_{ex} = \frac{|Ex_{Q_f}|}{|W_{cp}|}. \tag{36}$$

Within this structural definition, Ex_{Q_f} is credited as the useful liquefaction product, while C_{min}^{sch} remains a separately identified scheme-imposed contribution.

Normalizing the extended exergy balance in Equation (33) by the total mechanical-work input W_{cp} and using the definition in Equation (36) gives

$$\eta_{ex} = \frac{|Ex_{Q_f}|}{|W_{cp}|} = 1 - \frac{C_{min}^{sch} + \sum I_i + \sum L_i}{|W_{cp}|} = 1 - \Psi_{min}^{sch} - \sum \Psi_i, \tag{37}$$

where

$$\Psi_{min}^{sch} = \frac{C_{min}^{sch}}{|W_{cp}|} \text{ and } \Psi_i = \frac{I_i \text{ or } L_i}{|W_{cp}|}, \tag{38}$$

represent the shares of the scheme-imposed minimum thermodynamic consumption and of exergy destruction (I) or exergy loss (L), respectively, relative to the system's mechanical-work input.

The operating parameters are selected based on their impact on the exergy balance, with the aim of reducing mechanical-work consumption for a given cooling duty or liquefied flow rate.

2.3. Results

To evaluate the system performance, the influence of the design parameters p_1 (storage pressure) and p_2 (upper compression pressure) was analyzed for $p_0 = 0.1$ MPa and $T_1 = T_0 = 300$ K, considering a temperature difference at the warm end of the recuperative heat exchanger of $\Delta T_n = 6$ K and a compressor efficiency of $\eta_{cp,T} = 0.85$.

2.3.1. Influence of the Liquid Air Storage Pressure p_1

The variation in liquid fraction y and specific work consumption w_0 with storage pressure p_1 is shown in Figure 2a, and the variation in COP and structural liquefaction exergetic indicator η_{ex} is shown in Figure 2b.

It can be observed that increasing the storage pressure p_1 causes the liquid fraction to increase up to a maximum value, located around 0.9 MPa (Figure 2a). Beyond this value, increasing the storage pressure no longer produces a significant increase in the amount of liquid obtained. At the same time, the specific mechanical-work consumption w_0, expressed per kilogram of liquefied air, decreases as p_1 increases. From an energy perspective, this trend indicates a favorable effect of increasing the storage pressure, but only up to the point at which the liquid fraction reaches its maximum value.

The energetic coefficient of performance increases with p_1 (Figure 2b), following the favorable tendency indicated by the decrease in specific consumption. However, the exergy analysis reveals a different behavior: η_{ex} reaches a maximum in the range $p_1 \approx 0.4$–0.5 MPa, after which it starts to decrease. This distinction between the energy and the exergy criteria is important, as the pressure that maximizes the amount of liquid is not necessarily the pressure that ensures the most effective utilization of the available exergy. For the reference conditions adopted here, the exergetic maximum occurs near $p_1 = 0.4$ MPa and reflects the

trade-off between reduced throttling irreversibility and increasing compression- and heat-transfer-related contributions. Its location may shift when the ambient state, compressor efficiency, or insulation heat-ingress changes.

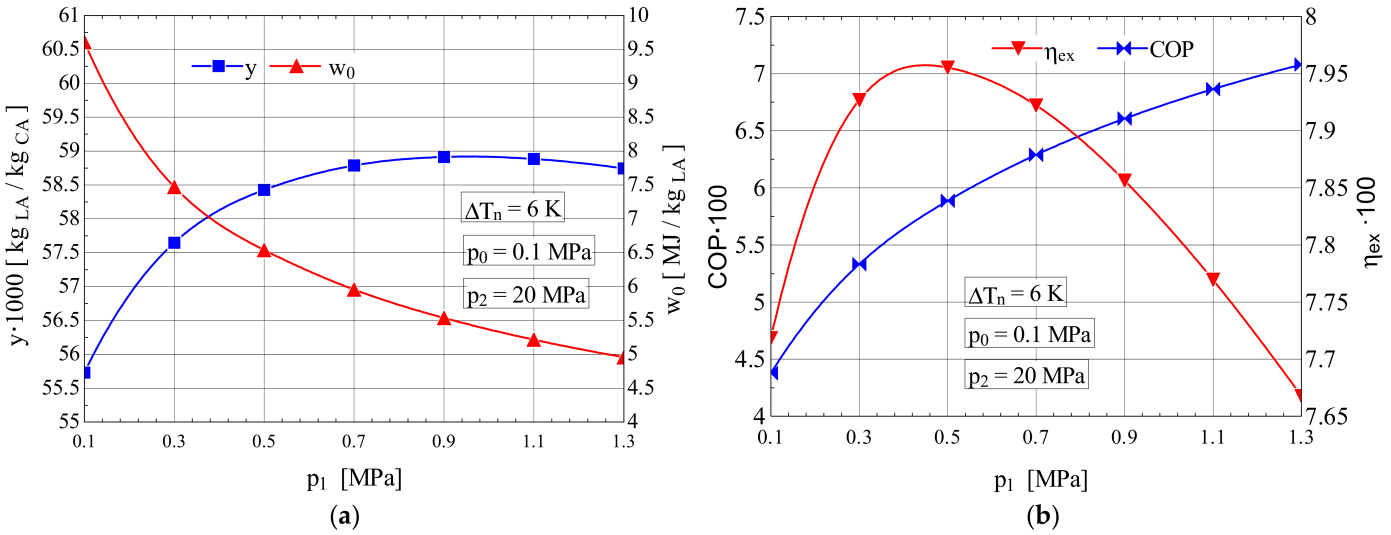


Figure 2. Influence of storage pressure p_1 on system performance: (**a**) variation in liquid fraction y and specific work consumption w_0; (**b**) variation in COP and structural liquefaction exergetic indicator η_{ex}.

Figure 3 summarizes the distribution of the scheme-imposed minimum thermodynamic consumption and exergy-destruction shares in the main components of the system for different values of the storage pressure p_1.

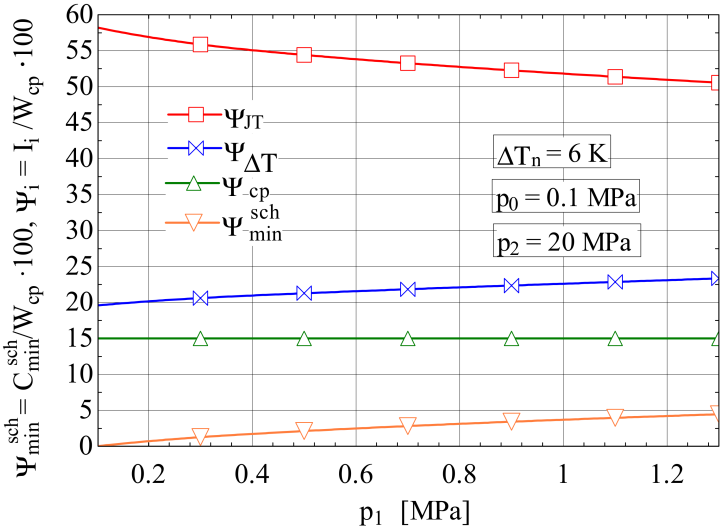


Figure 3. Variation in the normalized contributions in the structural exergy balance with p_1.

The distribution of exergetic losses explains the maximum observed in Figure 2b. The throttling valve remains the component with the highest share of exergy destruction (Ψ_{JT}), which is characteristic of Linde–Hampson cycles based on Joule–Thomson throttling. As p_1 increases, the throttling contribution (Ψ_{JT}) decreases, but this reduction is gradually counterbalanced by the increase in irreversibilities associated with heat transfer across finite temperature differences ($\Psi_{\Delta T}$) and with the scheme-imposed minimum thermodynamic consumption required to compress the make-up air from p_0 to p_1 $\left(\Psi_{min}^{sch}\right)$. Therefore, beyond the optimum region, the reduction in throttling losses is no longer sufficient to maintain an increase in the structural liquefaction exergetic indicator.

Figure 4 presents the influence of storage pressure p_1 on state 3 (Figure 1) of the compressed air at the inlet of the throttling valve.

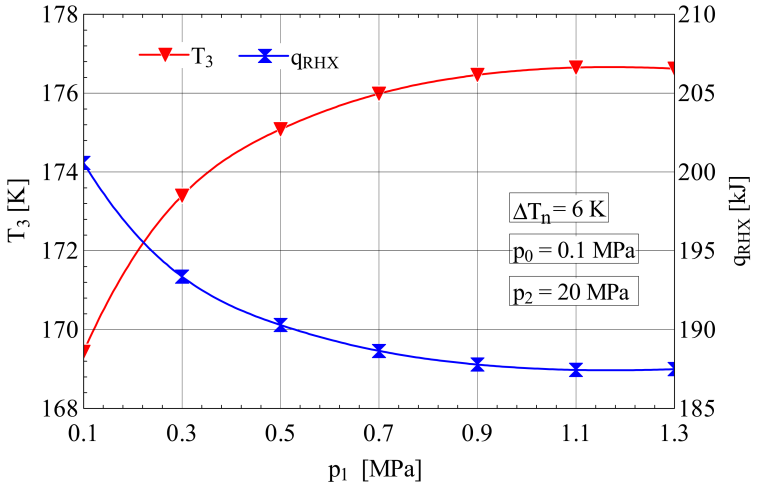


Figure 4. Influence of storage pressure p_1 on the temperature before throttling and on the recuperative heat duty.

It can be observed that temperature T_3 increases with increasing storage pressure (Figure 4). This increase indicates a change in the thermodynamic state of the working fluid before entering the throttling valve. At the same time, the heat duty of the recuperative heat exchanger decreases, showing that the heat exchanger transfers a smaller amount of heat as p_1 increases.

2.3.2. Influence of the Compression Pressure p_2

The study was performed for a liquid air storage pressure $p_1 = 0.4$ MPa, the value indicated by the maximum structural liquefaction exergetic indicator when p_1 is varied (Figure 2b).

The effects of the upper compression pressure p_2 on the liquid fraction y and specific work consumption w_0, as well as on COP and the structural liquefaction exergetic indicator, are presented in Figure 5a and Figure 5b, respectively.

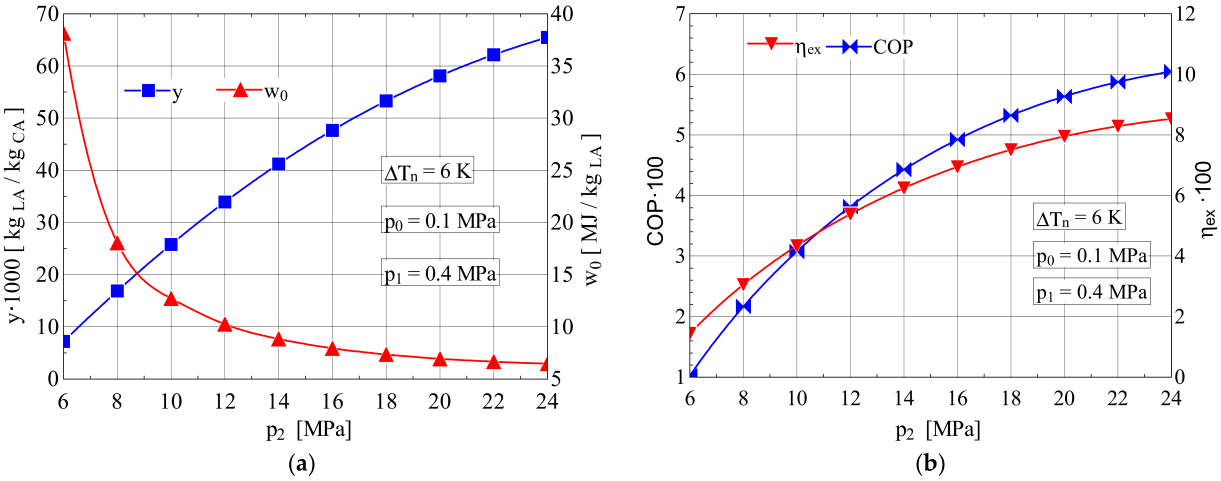


Figure 5. Influence of compression pressure p_2 on system performance: (**a**) variation in liquid fraction y and specific work consumption w_0; (**b**) variation in COP and structural liquefaction exergetic indicator η_{ex}.

Increasing the compression pressure p_2 leads to a marked increase in the liquid air fraction y and to a decrease in the specific mechanical-work consumption w_0 (Figure 5a).

It can be observed that, as the compression pressure p_2 increases, both performance coefficients, the energy coefficient (COP) and the structural liquefaction exergetic indicator (η_{ex}), increase continuously (Figure 5b). Compared with the influence of storage pressure, the effect of the upper compression pressure on the liquid fraction is more pronounced, highlighting the important role of the pressure level before throttling in the operation of the Linde–Hampson cycle.

The scheme-imposed minimum thermodynamic consumption and exergy-destruction shares in the system components as the compression pressure p_2 increases (Figure 6) show that the throttling valve continues to be the main source of exergy destruction (Ψ_{JT}), although its share decreases as p_2 increases. A decreasing trend is also observed for the irreversibilities associated with the recuperative heat exchanger ($\Psi_{\Delta T}$). In contrast, the contribution of the aggregate compressor–cooler (Ψ_{cp}) remains relatively stable under the imposed isothermal efficiency, while the contribution associated with make-up air compression shows only a limited increase (Ψ_{min}^{sch}). This redistribution of exergetic contribution shares explains the favorable evolution of the structural liquefaction exergetic indicator shown in Figure 5b.

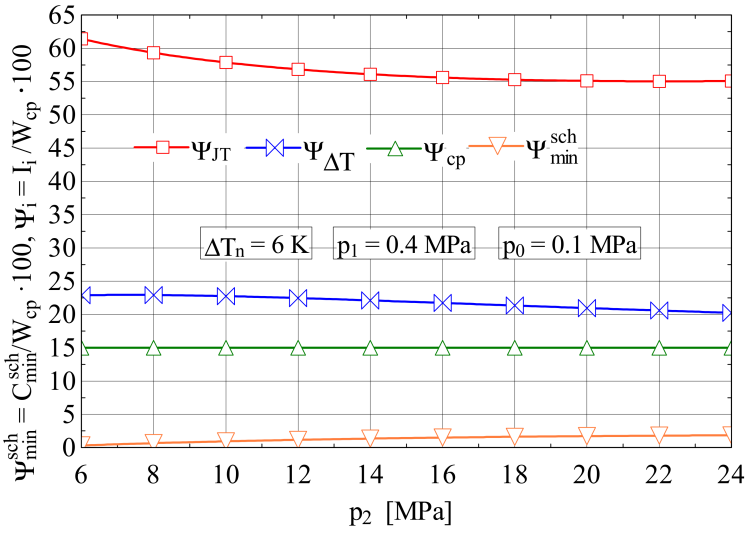


Figure 6. Variation in the normalized contributions in the structural exergy balance with p_2.

Overall, the results indicate that pressures p_1 and p_2 affect the performance of the single-throttling Linde–Hampson cycle differently. The exergy analysis indicates the existence of an optimum value of the storage pressure p_1 (Figure 2b). In contrast, increasing the upper compression pressure p_2 produces a monotonic increase in the COP and in the structural liquefaction exergetic indicator (η_{ex}) within the analyzed range (Figure 5). This tendency should not be extrapolated beyond the investigated interval, because higher compression pressures involve stricter mechanical design requirements, safety constraints, compressor loading, pressure-drop sensitivity, and capital cost. Thus, p_2 is treated here as a bounded thermodynamic design parameter rather than as an indefinitely increasing design variable. The dominant component of exergy destruction remains the throttling valve (Ψ_{JT}), while the recuperative heat exchanger also contributes significantly through the irreversibilities associated with heat transfer across a finite temperature difference ($\Psi_{\Delta T}$). Thus, parameter selection should be based on correlating the working pressures with a detailed analysis of exergetic consumptions, not only on maximizing the liquid fraction obtained.

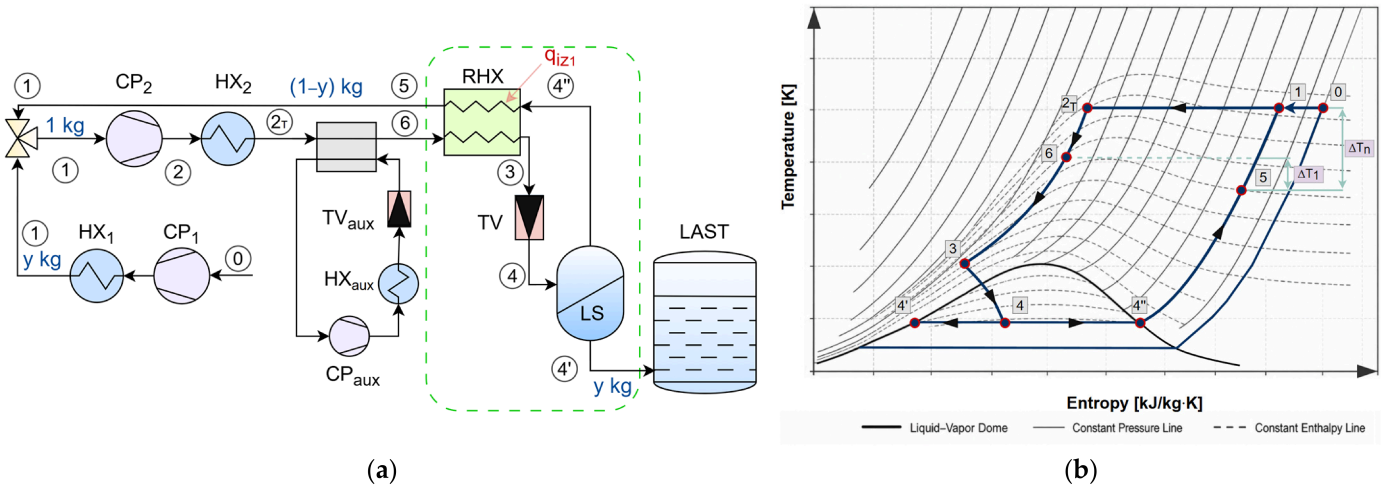
3. Linde–Hampson Cycle with an External Auxiliary Pre-Cooling Stage

To reduce the irreversibilities in the throttling valve, the first improvement in the Linde–Hampson scheme consists of introducing an auxiliary pre-cooling stage. If the compressed air enters the throttling valve at a lower temperature, state 3 (Figure 1) moves closer to the region in which the resulting liquid fraction after isenthalpic expansion is higher.

3.1. Schematic of the Linde–Hampson Cycle with an External Auxiliary Pre-Cooling Stage

The analysis is based on the initially proposed configuration, with a stage introduced to reduce the temperature of the high-pressure air by an equivalent auxiliary refrigeration block before it enters the recuperative heat exchanger (Figure 7a). A value of $f_{COP} = 0.60$ was adopted for the auxiliary subsystem in the reference case, consistent with simplified system-level models in which the actual refrigeration COP is represented as a fixed fraction of the reversed Carnot COP $COP_{real} = f_{COP} \cdot COP_C$ [26,27]. This factor is a comparative modeling assumption rather than a specification for a particular refrigeration plant, and the corresponding sensitivity analysis is reported in Supplementary Table S7. The subsystem is not resolved at the refrigerant-cycle or equipment level; T_6 and T_7 are therefore imposed thermodynamic pre-cooling levels. Near 200 K, implementation would generally require a cascaded or cryogenic refrigeration architecture and may yield a lower effective COP. Decreasing the imposed pre-cooling temperature shifts state 3 toward lower enthalpy and reduces throttling irreversibility because the exergy degradation process occurs at a more favorable thermodynamic level (Figure 7b).

The system layout and the schematic T–s diagram are shown in Figure 7a and Figure 7b, respectively.



(**a**) (**b**)

Figure 7. Linde–Hampson air liquefaction system with auxiliary pre-cooling of the main air stream from ambient temperature: (**a**) system layout; (**b**) schematic T–s diagram of the proposed cycle (not to scale).

3.2. Mathematical Modeling of the Linde–Hampson Cycle with an External Auxiliary Pre-Cooling Stage

The mathematical model is implemented within the same computational framework in EES, which integrates both energy and exergy analyses.

3.2.1. Energy Analysis for Linde–Hampson Cycle with an External Auxiliary Pre-Cooling Stage

To determine the liquefied air fraction y, the energy balance is written for the green boundary of the cold zone (Figure 7), for a unit mass of gas entering RHX at state 6. The liquid fraction produced after throttling and separation is

$$y = \frac{h_6 - h_5 + q_{iz}}{h_{4'} - h_5}. \tag{39}$$

If relations (2)–(4) are considered and the specific cooling duty supplied by the auxiliary system for pre-cooling the main air stream from state 2_T to state 6 is denoted by $q_{aux} = h_{2_T} - h_6$, relation (39) can be written as

$$y = \frac{|\Delta h_{T,1-2_T}| + q_{aux} - q_n - q_{iz}}{q_f - q_n}. \tag{40}$$

The coefficient of performance of the Linde–Hampson cycle with external auxiliary pre-cooling is given by

$$COP = \frac{Q_f}{|W_{cp}| + |W_{cp}^{aux}|} = \frac{y \cdot (q_f - q_n)}{|W_{cp,1}| + |w_{cp,2}| + |W_{cp}^{aux}|}, \tag{41}$$

where

$$|w_{cp,2}| = \frac{|w_{cp,T_0}^{1-2_T}|}{\eta_{cp,T}}, |W_{cp,1}| = \frac{y|w_{cp,T_0}^{0-1}|}{\eta_{cp,T}} \text{ and } |W_{cp}^{aux}| = \frac{q_{aux}}{COP_{real}}. \tag{42}$$

The specific mechanical work required to produce 1 kg of liquefied air is

$$w_0 = \frac{|w_{cp,T_0}^{1-2_T}| + y|w_{cp,T_0}^{0-1}|}{\eta_{cp,T} \cdot y} + \frac{|W_{cp}^{aux}|}{y} = \frac{|W_{cp}| + |W_{cp}^{aux}|}{y}. \tag{43}$$

3.2.2. Exergy Analysis for Linde–Hampson Cycle with an External Auxiliary Pre-Cooling Stage

Assuming negligible pressure losses in the recuperative heat exchanger, the exergy balance equation applied to the green dashed boundary in Figure 7 can be written as

$$Ex_6 + Ex_{Qiz} = Ex_{4'} + Ex_5 + i_{JT} + I_{\Delta T}, \tag{44}$$

Apart from Ex_6, the calculation of all other terms in Equation (44) follows the reasoning presented in Section 2.

For 1 kg of gas compressed in CP_2, the exergy at state 6 is written as

$$Ex_6 = 1 \cdot ex_6 = ex_6 - ex_0 = h_6 - h_0 - T_0(s_6 - s_0). \tag{45}$$

The specific exergy of state 6, $ex_6(T_6, p_2)$, is thermomechanical. To separate these components, the system is considered to follow the reversible path $(6 - 2_T - 0)$ on its way to thermomechanical equilibrium with the ambient environment. Thus,

$$ex_6 = (h_6 - h_{2_T}) + (h_{2_T} - h_0) - T_0[(s_6 - s_{2_T}) + (s_{2_T} - s_0)] = ex_6^T + ex_6^M. \tag{46}$$

The thermal component is given by

$$ex_6^T = h_6 - h_{2_T} - T_0(s_6 - s_{2_T}) = (h_6 - h_{2_T})\left(1 - \frac{T_0}{T_{m,6-2_T}}\right), \tag{47}$$

and represents the minimum mechanical work required for the auxiliary system to cool 1 kg of air from $2_T(T_0, p_2)$ to $6(T_6, p_2)$. Therefore,

$$ex_6^T = \left|ex_{q_{6-2_T}}^{T_{m,6-2_T}}\right| = |w_{min}^{aux}|. \quad (48)$$

The mechanical component of the exergy of state 6 is given by

$$ex_6^M = h_{2_T} - h_0 - T_0(s_{2_T} - s_0) = \left|w_{cp,T_0}^{0-2_T}\right|, \quad (49)$$

corresponding to the minimum mechanical work consumed in an isothermal compression process at T_0 for 1 kg of air, from p_0 to p_2.

Substituting Equations (45)–(49) and (13)–(23) into Equation (44) yields

$$|w_{min}^{aux}| + \left|w_{cp,T_0}^{0-2_T}\right| - L_{Qiz} = |Ex_{Qf}| + y\left|w_{cp,T_0}^{0-1}\right| + L_{Qn} + (1-y)\left|w_{cp,T_0}^{0-1}\right| + i_{JT} + I_{\Delta T}\,. \quad (50)$$

By separating on the left-hand side of Equation (50) what is consumed to extract the liquefaction cooling duty of the fraction y of liquid air $|Ex_{Qf}|$, one obtains

$$|w_{min}^{aux}| + \left|w_{cp,T_0}^{0-2_T}\right| - (1-y)\left|w_{cp,T_0}^{0-1}\right| = |Ex_{Qf}| + y\left|w_{cp,T_0}^{0-1}\right| + i_{JT} + I_{\Delta T} + L_{Qn} + L_{Qiz}. \quad (51)$$

The minimum work of the auxiliary pre-cooling system is evaluated from the exergy of the heat extracted from the main air stream, considering a reversed Carnot cycle between the mean cooling temperature $T_{m,6-2_T}$ and the ambient temperature T_0. Thus, $\left|ex_{q,6-2_T}\right| = |W_{min}^{aux}|$. Assuming $COP_{real} \simeq 0.6COP_C$, $\left|W_{cp}^{aux}\right| = \frac{h_{2_T}-h_6}{0.6COP_C}$, with $COP_C = \frac{T_6}{T_0-T_6}$.

Treating the main and auxiliary compression systems as aggregate compressor–cooler assemblies, Equation (51) may be expressed as

$$\left|W_{cp}^{aux}\right| + |W_{cp}| = |Ex_{Qf}| + C_{min}^{sch} + i_{JT} + I_{\Delta T} + I_{cp,2} + \left|Ex_{Qcp_2}\right| + I_{cp,1} + \left|Ex_{Qcp_1}\right| + I_{cp}^{aux} + \left|Ex_Q^{aux}\right| + L_{Qiz} + L_{Qn} \quad (52)$$

where

$$I_{cp}^{aux} + \left|Ex_Q^{aux}\right| = \left|W_{cp}^{aux}\right| - |W_{min}^{aux}|. \quad (53)$$

For the externally pre-cooled configuration, the structural liquefaction exergetic indicator becomes

$$\eta_{ex} = \frac{|Ex_{Q_f}|}{|W_{cp}| + \left|W_{cp}^{aux}\right|}. \quad (54)$$

The shares of the scheme-imposed minimum thermodynamic consumption and of the exergy destruction (I) or exergy loss (L), respectively, relative to the system's mechanical-work input are

$$\Psi_{min}^{sch} = \frac{C_{min}^{sch}}{|W_{cp}| + \left|W_{cp}^{aux}\right|},\ \Psi_i = \frac{I_i \text{ or } L_i}{|W_{cp}| + \left|W_{cp}^{aux}\right|}. \quad (55)$$

3.3. Results for Linde–Hampson Cycle with an External Auxiliary Pre-Cooling Stage

The influence of the design parameter T_6 (external auxiliary pre-cooling temperature) was investigated, while preserving the assumptions adopted for the simple Linde–Hampson cycle: $p_1 = 0.4$ MPa, $p_2 = 20$ MPa, $\Delta T_n = 6$ K, and reference state $0 \equiv (T_0,\ p_0)$.

The analysis indicates that decreasing the temperature T_6 has a pronounced positive effect on the energy performance of the liquefaction cycle (Figure 8a). Over the analyzed range, $T_6 = 280$–220 K, the liquid air fraction y increases from approximately 76.8‰ to 175.4‰, corresponding to an increase of about 128.3%. Over the same inter-

val, the specific mechanical work required to obtain 1 kg of liquefied air decreases by approximately 2.542 MJ/kg_{LA}. This result shows that the increase in liquid production significantly compensates for the additional mechanical work required to operate the auxiliary refrigeration system.

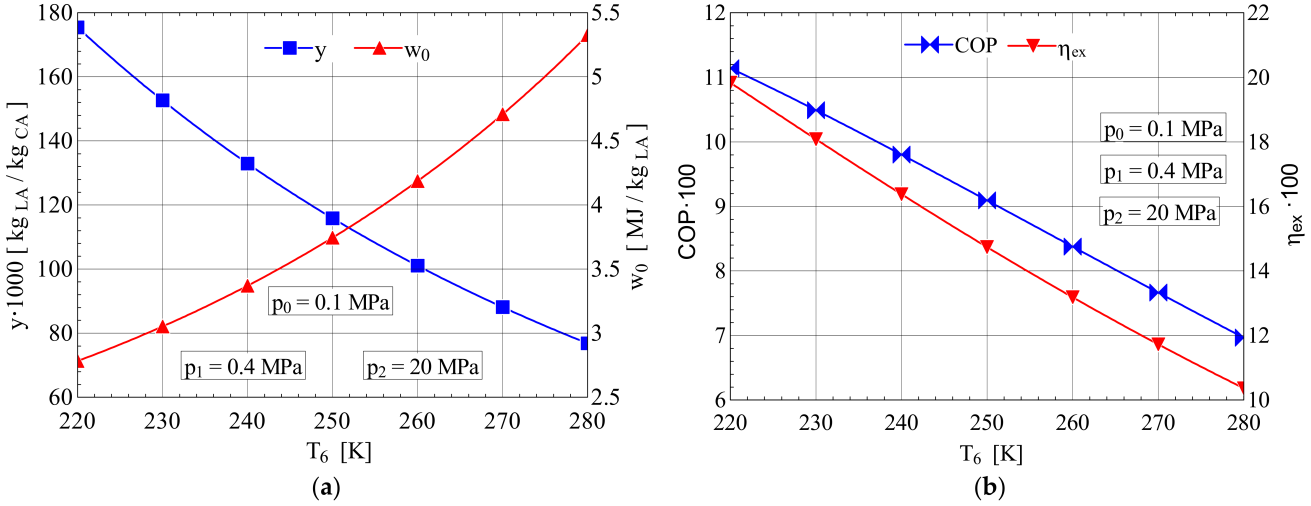


Figure 8. Influence of the external auxiliary pre-cooling temperature T_6 on system performance: (**a**) variation in liquid fraction y and specific work consumption w_0; (**b**) variation in COP and structural liquefaction exergetic indicator η_{ex}.

The energy and exergy performance indicators shown in Figure 8b follow the same trend. COP increases by approximately 4.18 percentage points on the COP · 100 scale, while η_{ex} increases by 9.47 percentage points. These results show that the improvement is not only energetic but also exergetic: the supplied mechanical work is converted more efficiently into the useful liquefaction effect.

The reduction in throttling irreversibility is the main mechanism behind this improvement (Figure 9). The share of exergy destruction associated with the throttling valve decreases from 53.07% at $T_6 = 280$ K to 39.13% at $T_6 = 220$ K. At the same time, the exergy destruction associated with heat transfer across a finite temperature difference in the recuperative heat exchanger decreases from 19.33% to 11.59%. These two reductions explain the increase in the structural liquefaction exergetic indicator of the cycle.

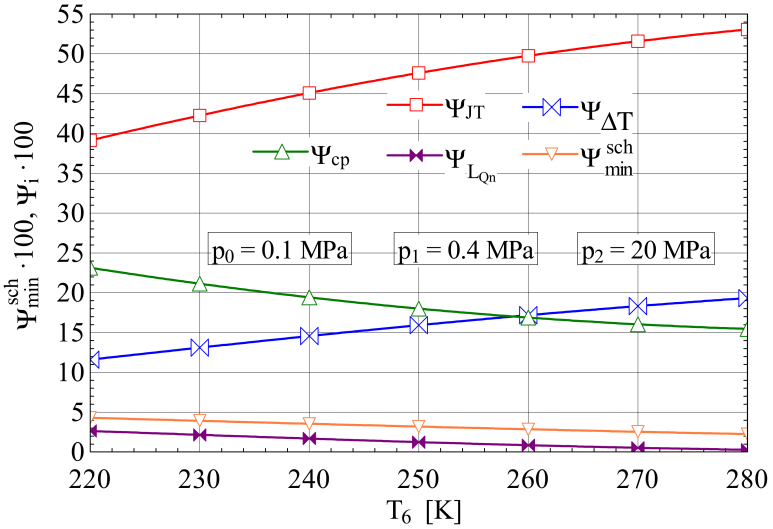


Figure 9. Variation in the normalized contributions in the structural exergy balance with the external auxiliary pre-cooling temperature T_6.

However, the results also reveal the cost of the modification. As T_6 decreases, the contribution of the aggregate compressor–cooler contribution (Ψ_{cp}) increases from 15.45% to 23.14%, because the compressor of the auxiliary refrigeration system is increasingly loaded. In addition, the exergy loss L_{Qn}, associated with the external heating of the secondary stream from state 5 to state 1, becomes non-negligible (Figure 10), with an increase from 1.119 to 12.85 kJ/kg$_{CA}$. The heat absorbed by this stream from the external environment increases from 24.29 to 71.89 kJ/kg$_{CA}$ over the analyzed range. This behavior shows that part of the cold potential of the return stream is not recovered internally in the cycle.

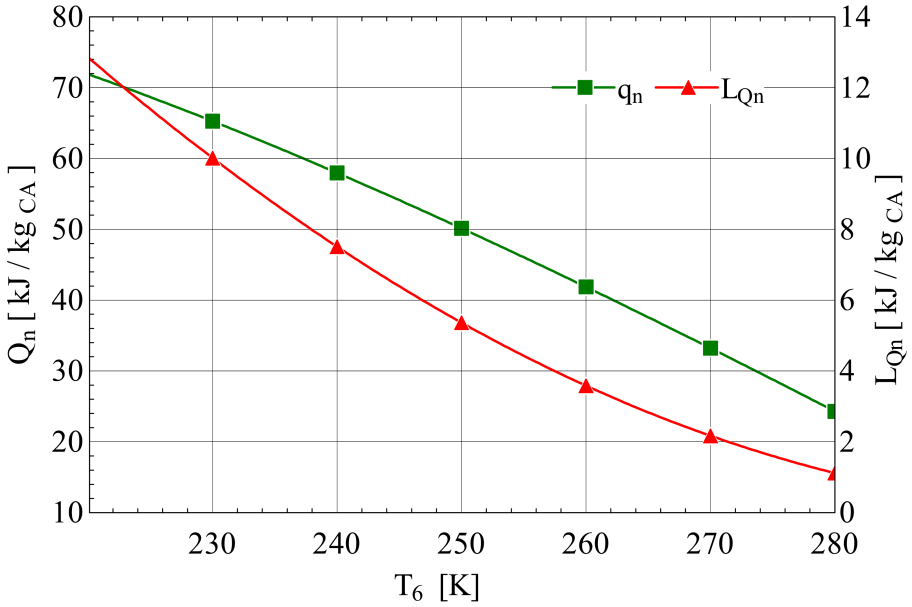
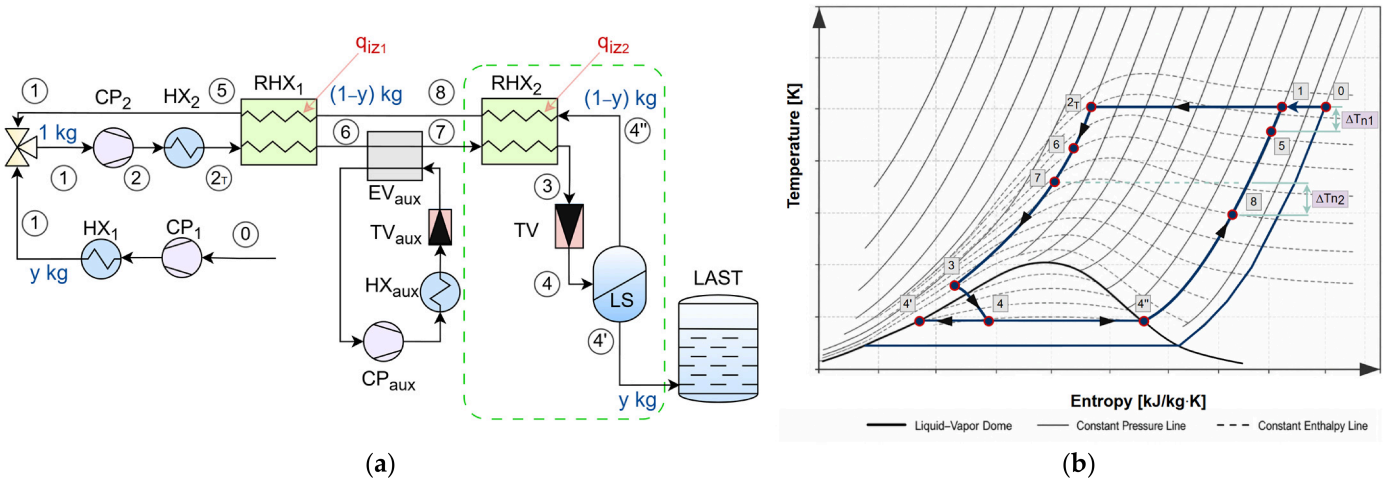


Figure 10. Influence of the external auxiliary pre-cooling temperature T_6 on the exergy loss L_{Qn} and on the heat Q_n associated with external heating of the secondary stream from state 5 to state 1.

Consequently, the Linde–Hampson cycle with external auxiliary pre-cooling represents a clear improvement over the simple cycle, but it also reveals a new limitation. By reducing T_6, the cycle decreases throttling losses and improves liquefaction performance; however, the modified thermal profile causes the secondary stream to leave the recuperator at a temperature far below ambient temperature. The low temperature of the return stream at state 5 indicates that part of its cold exergy remains unrecovered and is lost as the stream is heated to state 1 through interaction with the environment (Figures 7b and 10). This result provides the thermodynamic justification for a further structural improvement—the introduction of an additional recuperative heat exchanger—so that more of the return-stream cold exergy is recovered internally rather than lost to the environment.

4. Linde–Hampson Cycle with Two Recuperative Heat Exchangers and Intermediate Auxiliary Pre-Cooling

Compared with the previous configuration, staged thermal recovery is introduced using two recuperative heat exchangers, RHX_1 and RHX_2 (Figure 11), with the auxiliary refrigeration system located between them. Thus, the high-pressure stream is no longer cooled by the auxiliary system immediately after HX_2 but is first cooled recuperatively in RHX_1, from state 2_T to state 6. It is then cooled in the evaporator of the auxiliary refrigeration system EV_{aux}, from state 6 to state 7, after which it enters the second recuperative stage, RHX_2, where it reaches state 3 before isenthalpic throttling in the throttling valve.



(**a**) (**b**)

Figure 11. The Linde–Hampson liquefaction system with two recuperative heat exchangers and intermediate auxiliary pre-cooling: (**a**) system layout; (**b**) illustrative T–s diagram of the proposed cycle (not to scale).

4.1. Schematic of the Linde–Hampson Liquefaction System with Two Recuperative Heat Exchangers and Intermediate Auxiliary Pre-Cooling

The system layout and the representation of the cycle in the T–s diagram are shown in Figure 11a and Figure 11b, respectively.

4.2. Mathematical Modeling of the Linde–Hampson Cycle with Two Recuperative Heat Exchangers and Intermediate Auxiliary Pre-Cooling

The mathematical model is implemented within the same computational framework in EES, in which both energy and exergy analyses are integrated.

4.2.1. Energy Analysis of the Linde–Hampson Cycle with Two Recuperative Heat Exchangers and Intermediate Auxiliary Pre-Cooling

From the energy balance equation applied to the throttling-stage boundary (green dashed line in Figure 11a), the liquid air fraction produced per kilogram of compressed air is obtained:

$$y = \frac{h_7 - h_8 + q_{iz_2}}{h_{4'} - h_8}. \quad (56)$$

This relation highlights the direct influence of pre-cooling on liquid production. Reducing the temperature of state 7 changes the inlet enthalpy of heat exchanger RHX_2 and shifts state 3 toward lower temperatures, thereby increasing the liquid fraction after throttling. This increase requires additional auxiliary refrigeration work along paths 6–7; therefore, the specific work per kilogram of liquid air includes both the main air-compression input and the auxiliary input defined in Equation (43). Across all investigated p_1, p_2, T_6, and T_7 values, the local temperature difference remained positive, with an approximately 6 K minimum at the warm end; the complete verification is reported in Supplementary Table S9.

4.2.2. Exergy Analysis of the Linde–Hampson Cycle with Two Recuperative Heat Exchangers and Intermediate Auxiliary Pre-Cooling

The exergy analysis highlights the distribution of exergy destruction and losses throughout the cycle. The system releases heat at a temperature level above the ambient temperature ($T > T_0$) through the compressor coolers and receives heat below ambient temperature ($T < T_0$) through the imperfect insulation of the two recuperative heat exchangers.

By enclosing the entire system within a boundary separating it from the ambient environment, the interactions between the system and its ambient environment are identified. The conceptual scheme of these interactions is presented in Figure 12.

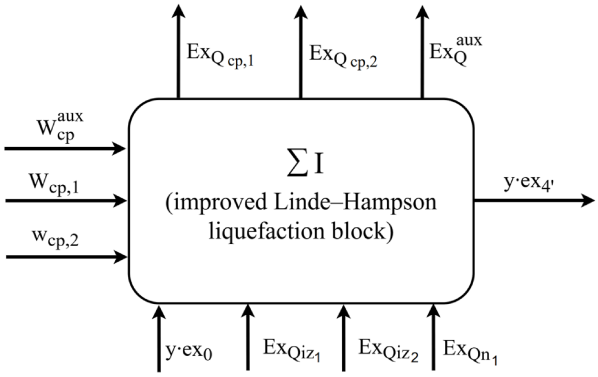


Figure 12. Exergetic interactions of the improved two-RHX liquefaction block with the environment.

The exergy balance equation applied to the assembly formed by the air liquefaction system and the auxiliary pre-cooling system for the main air stream is written as

$$\sum Ex_Q = \Delta Ex + \sum W + \sum I \tag{57}$$

According to the scheme in Figure 12, the terms in Equation (57) are expressed as

$$\sum Ex_Q = Ex_{Qcp_1} + Ex_{Qcp_2} + Ex_Q^{aux} + Ex_{Qiz_1} + Ex_{Qiz_2} + Ex_{Qn_1} = -\left|Ex_{Qcp_1}\right| - \left|Ex_{Qcp_2}\right| - \left|Ex_Q^{aux}\right| - \left|Ex_{Qiz_1}\right| - \left|Ex_{Qiz_2}\right| - \left|Ex_{Qn_1}\right|. \tag{58}$$

It can be observed that heat is rejected to the ambient environment in the compressor coolers $\left(Q_{cp} < 0\right)$ at a temperature $T > T_0$; the heat rejected by the system is negative, while its exergetic factor is positive, which gives these exergy terms a negative sign $\left(\theta_Q = \left(1 - \frac{T_0}{T}\right), T > T_0 \Rightarrow \theta_Q > 0\right)$.

For the heat entering through the insulation of the heat exchangers, the sign of the heat is positive, but the temperature at which it is received by the system is $T < T_0$; consequently, the sign of the exergetic factor is negative, as is the sign of the exergy of the heat received in this case. The same occurs for the cold gas at the outlet of the first recuperative heat exchanger: because the temperature difference ΔT_{n1} is imposed at the warm end, the cold gas at state 5 receives the heat Q_n from the ambient environment instead of receiving it from the main air stream, which is clearly a loss. The exergy associated with this heat transfer to the air stream at a temperature below T_0 is therefore negative.

The exergy change in the material streams between the system inlet and outlet is

$$\Delta Ex = y(ex_{4'} - ex_0) = y[(ex_{4'} - ex_1) + (ex_1 - ex_0)]. \tag{59}$$

Considering Equations (22), (23), and (32), Equation (59) takes the form

$$\Delta Ex = \left|Ex_{Q_f}\right| + C_{min}^{sch}. \tag{60}$$

Since the mechanical-work terms exchanged with the surroundings represent inputs to the system, they carry a negative sign:

$$\sum W = W_{cp_1} + w_{cp_2} + W_{cp}^{aux} = -\left|W_{cp_1}\right| - \left|w_{cp_2}\right| - \left|W_{cp}^{aux}\right|. \tag{61}$$

The internal destruction terms are grouped as follows:

$$\sum I = I_{cp,1} + I_{cp,2} + I_{cp}^{aux} + i_{JT} + I_{\Delta T_1} + I_{\Delta T_2} + I_{\Delta T}^{aux} + \sum I_{aux}, \tag{62}$$

Substituting relations (58)–(62) into Equation (57) gives

$$\begin{aligned}\left|W_{cp_1}\right| + \left|w_{cp_2}\right| + \left|W_{cp}^{aux}\right| = {} & \left|Ex_{Qf}\right| + C_{min}^{sch} + I_{cp,1} + \left|Ex_{Qcp_1}\right| + I_{cp,2} + \left|Ex_{Qcp_2}\right| + I_{cp}^{aux} \\ & + \left|Ex_{Q}^{aux}\right| + \left|Ex_{Qiz_1}\right| + \left|Ex_{Qiz_2}\right| + \left|Ex_{Qn_1}\right| + i_{JT} + I_{\Delta T_1} + I_{\Delta T_2} + I_{\Delta T}^{aux} + \sum I_{aux}.\end{aligned} \tag{63}$$

The heat flows exchanged by the system with the ambient environment represent losses. If heat transfer occurs at $T > T_0$, this is the loss of mechanical work that could have been obtained with a direct Carnot cycle; if heat is received at $T < T_0$, it must be extracted from the system and is added to the cooling duty, thereby consuming minimum mechanical work in a refrigeration machine operating according to a reversed Carnot cycle.

Classifying the external heat–exergy interactions as losses, Equation (63) takes the form

$$\begin{aligned}\left|W_{cp_1}\right| + \left|w_{cp_2}\right| + \left|W_{cp}^{aux}\right| = {} & \left|Ex_{Qf}\right| + C_{min}^{sch} + I_{cp,1} + \left|Ex_{Qcp_1}\right| + I_{cp,2} + \left|Ex_{Qcp_2}\right| + I_{cp}^{aux} + \left|Ex_{Q}^{aux}\right| + L_{Qiz_1} + L_{Qiz_2} + L_{Qn_1} + i_{JT} \\ & + I_{\Delta T_1} + I_{\Delta T_2} + I_{\Delta T}^{aux} + \sum I_{aux}.\end{aligned} \tag{64}$$

The heat entering through the insulation of the recuperative heat exchangers is treated as an exergy loss because it must be removed, directly or indirectly, from the cryogenic domain. For HX_1 and HX_2, one obtains

$$L_{Qiz_1} = q_{iz_1}\left(\frac{T_0}{T_{m,8-5}} - 1\right), \text{and } L_{Qiz_2} = q_{iz_2}\left(\frac{T_0}{T_{m,4''-8}} - 1\right). \tag{65}$$

The loss $L_{Qn_1} = L_{\Delta T_n}$, caused by heating the secondary stream from state 5 to state 1 through contact with the ambient environment rather than by cooling the primary stream, is calculated using Equation (17).

In the two recuperative heat exchangers, exergy destruction occurs because of heat transfer across a finite temperature difference. For HX_1 and HX_2, one obtains

$$I_{\Delta T_1} = T_0\left[s_6 + (1-y)s_5 - s_{2_T} - (1-y)s_8 - \frac{q_{iz_1}}{T_{m,8-5}}\right], \tag{66}$$

$$I_{\Delta T_2} = T_0\left[s_3 + (1-y)s_8 - s_7 - (1-y)s_{4''} - \frac{q_{iz_2}}{T_{m,4''-8}}\right]. \tag{67}$$

The exergy destruction associated with the finite temperature difference in the auxiliary heat exchanger (for the ideal case $T_{EV}^{aux} = T_7$) is

$$I_{\Delta T}^{aux} = (h_6 - h_7)\frac{T_{m,6-7} - T_{EV}^{aux}}{T_{EV}^{aux} \cdot T_{m,6-7}}. \tag{68}$$

4.3. Analysis of the Influence of the Auxiliary Evaporator Outlet Temperature T_7

The numerical analysis was carried out for the Linde–Hampson cycle with two recuperative heat exchangers and intermediate auxiliary pre-cooling, maintaining the pressures $p_0 = 0.1$ MPa, $p_1 = 0.4$ MPa, and $p_2 = 20$ MPa, for $T_1 = 300$ K, $\Delta T_n = 6$ K, and $\eta_{cp,T} = 0.85$. The variable parameter is temperature T_7, defined as the outlet temperature of the high-pressure air stream leaving the auxiliary evaporator. This temperature characterizes the pre-cooling level imposed by the auxiliary refrigeration system before the stream enters the cryogenic zone of the cycle.

Reducing T_7 from 280 K to 200 K increases the liquid fraction from 76.81 to 231.9 $kg_{LA}/(1000 \cdot kg_{CA})$, corresponding to an increase of 201.91%. Over the same interval, the specific mechanical work decreases from 5.301 to 2.099 MJ/kg_{LA}, i.e., by 60.4% (Figure 13a). Although the total mechanical work supplied to the cycle increases from 407.156 to 486.868 kJ/kg_{CA}, the much larger increase in liquid production reduces the work consumption per one kilogram of liquefied air. This relation confirms that the pre-cooling

level before cryogenic recovery is one of the dominant parameters of the scheme. At lower temperatures, the thermodynamic state before throttling is shifted toward a lower enthalpy, and the Joule–Thomson expansion produces a larger liquid fraction. Simultaneously, because the produced liquid mass increases, the mechanical consumption per unit of liquefied product decreases.

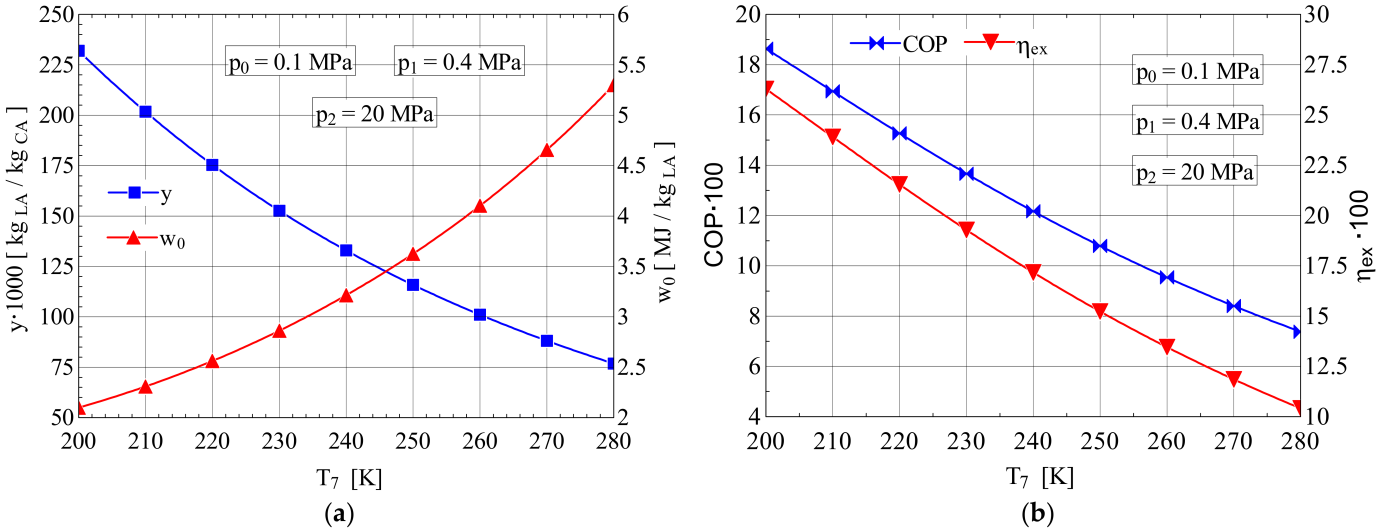


Figure 13. Influence of the auxiliary evaporator outlet temperature T_7 on system performance: (**a**) variation in liquid fraction y and specific work consumption w_0; (**b**) variation in COP and structural liquefaction exergetic indicator η_{ex}.

Figure 13b shows that reducing temperature T_7 increases COP by 152.47% and the structural liquefaction exergetic indicator by 152.55%, in relative terms, within the investigated interval. The similar relative increases in COP and η_{ex} indicate that the improvement in energy performance is accompanied by a more effective conversion of the supplied mechanical work into a useful liquefaction effect. Within the investigated T_7 interval, both COP and exergetic efficiency increase monotonically as T_7 decreases; therefore, no interior optimum is identified under the adopted auxiliary refrigeration model. An equipment-level optimum may differ because the achievable auxiliary COP, refrigeration architecture, and system complexity vary with temperature.

Figure 14 illustrates the distribution of the exergy-destruction and exergy-loss shares used in the exergetic analysis of the scheme. Decreasing temperature T_7 causes a significant reduction in the share of exergy destruction associated with throttling, from 53.31% at $T_7 = 280$ K to 36.33% at $T_7 = 200$ K. Nevertheless, throttling remains the main source of irreversibility in the cycle over the entire investigated range.

The share of exergy destruction generated by finite temperature differences in the recuperative heat exchangers also exhibits a favorable evolution. The total contribution of the two recuperative heat exchangers decreases from 18.26% to 10.52%, mainly because of the recuperative heat exchanger RHX_2, for which the contribution decreases from 18.10% to 8.272%. In contrast, the contribution of RHX_1 increases from 0.1585% to 2.252%, but this increase is much smaller than the reduction obtained in RHX_2. Therefore, reducing T_7 not only affects the throttling process but also improves the overall thermal matching in the low-temperature zone.

In parallel with the reduction in the shares associated with throttling and internal heat transfer, reducing T_7 increases the share of aggregate compressor–cooler contribution from 15.08% to 18.04%. The normalized contribution of the scheme-imposed minimum thermodynamic consumption, Ψ_{min}^{sch}, also increases from 2.251% to 5.685%, because a larger liquid air fraction is produced. Physically, this correlation is expected: as pre-cooling

reduces the dominant irreversibilities in throttling and in the recuperative heat exchangers, the relative contribution of compression becomes more visible, and the scheme-imposed minimum consumption term acquires a larger share in the normalized balance. Therefore, the increase in these two terms does not indicate a deterioration of global performance, but rather a redistribution of exergetic shares resulting from the reduction in the dominant sources of irreversibility in the cryogenic zone.

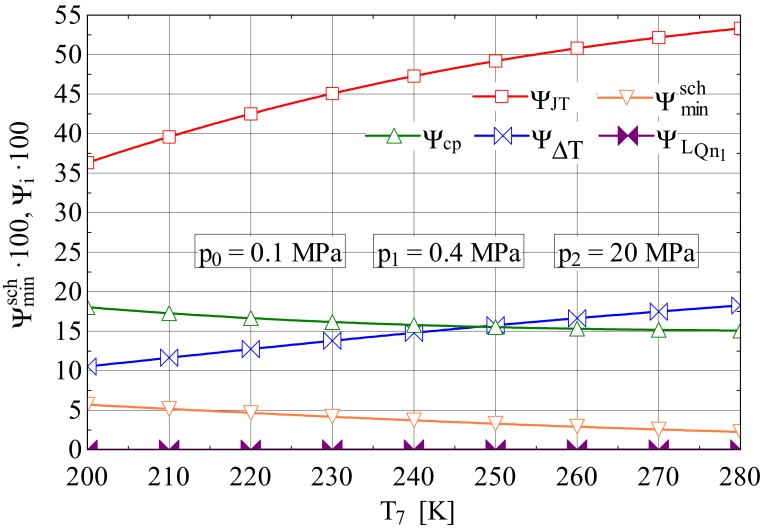


Figure 14. Variation in the normalized contributions in the structural exergy balance with the auxiliary evaporator outlet temperature T_7.

Finally, to assess the influence of the compressor representation, the three reference liquefaction configurations were also evaluated using a finite-stage intercooled real-gas model. The comparison, reported in Supplementary Table S12, shows that the finite-stage representation reduces the absolute COP values and the values of the structural liquefaction exergetic indicator, while preserving the relative ranking of the three configurations.

5. Energy Recovery Stage

The liquid air produced by the Linde–Hampson plant with two recuperative heat exchangers and intermediate auxiliary pre-cooling is stored in the liquid air storage tank (LAST) at an elevated pressure $p_1 = 0.4$MPa, as saturated liquid (state 4′). Before expansion, the fluid must be brought to a gaseous state with high energy potential, which requires increasing both its pressure and its temperature.

5.1. Schematic of the Energy Recovery Stage

The system layout and the cycle in the T–s diagram are shown in Figure 15a and Figure 15b, respectively.

The process is described by a sequence of transformations. Liquid air is pumped adiabatically to a high pressure by means of a cryogenic liquid pump P (4′–9), after which staged regasification takes place. Regasification begins with air heating (9–10) in heat exchanger HX_3, using a water stream initially at ambient temperature, followed by additional heating (10–11) in heat exchanger HX_4 using a waste-heat stream. The regasified air, now with high energy potential, is then expanded in turbine tur (11–12), where useful mechanical work is produced.

The waste-heat stream is treated as an external thermal stream available at a temperature level sufficient to impose the selected turbine inlet temperature and is modeled as an equivalent sensible-heat carrier with constant $c_{p,g}$ and without a resolved chemical composition. Only its physical-exergy change during cooling is included; upstream gener-

ation and chemical exergy lie outside the adopted system boundary. The reference inlet temperature is 700 K, and the attainable turbine inlet temperature T_{11} depends on both the source temperature and its heat-capacity rate. Depending on the integration site, this thermal input may be supplied by flue gas, hot process gas, thermal oil, or another industrial residual-heat carrier [28]. Industrial exhaust streams at temperature levels relevant to the present analysis are documented in energy-intensive sectors; for example, glass-melting furnace exhaust gases have been reported in the range 200–650 °C [29]. Therefore, the discharge stage is interpreted as an integrated LAES recovery unit coupled to an available waste-heat source.

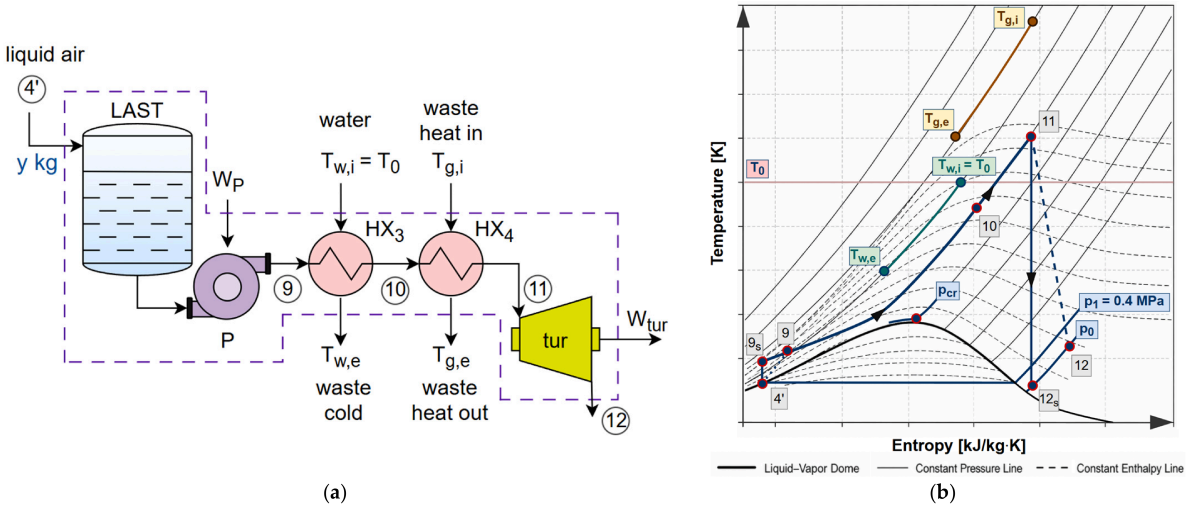


Figure 15. Energy recovery stage of LAES system: (**a**) System layout; (**b**) Cycle representation in the T–s diagram.

5.2. Mathematical Modeling of the Energy Recovery Stage

A continuous nominal operating regime is adopted for performance analysis. Thus, the stored liquid air fraction continuously feeds the discharge stage. All specific quantities in the recovery stage are normalized per kilogram of air entering the liquefaction block; therefore, the liquid air mass available for discharge is y kg_{LA}/kg_{CA}. If charging and discharging are operated with different mass flow rates or durations, the total power output and cooling capacity scale with those operating conditions, whereas the specific exergetic indicators remain comparable only on this common mass basis. Partial-load operation may also change turbomachinery efficiencies and heat-exchanger temperature profiles; therefore, the present values correspond to nominal steady-state operation.

5.2.1. Single-Stage Adiabatic Expansion

The exergy balance of the discharge stage is applied to the purple boundary (Figure 15a), which separates the system from the environment; the corresponding balance is shown in Figure 16.

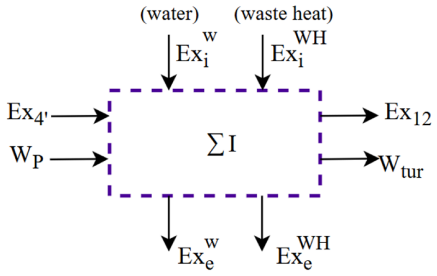


Figure 16. Exergy balance applied to the energy recovery assembly.

There is no explicit heat interaction across the selected external boundary of the system; the thermal exergy used in the heating-regasification processes of liquid air is included in the total exergy of the material streams in the balances of heat exchangers HX_3 and HX_4. Thus

$$\sum Ex_Q = 0. \tag{69}$$

Consequently, the exergy balance becomes

$$0 = \Delta Ex + \sum W + \sum I. \tag{70}$$

The remaining terms in Equation (70) are detailed as follows:

$$\Delta Ex = Ex_e^w - Ex_i^w + Ex_e^{WH} - Ex_i^{WH} + Ex_{12} - Ex_{4'}, \tag{71}$$

where

$$Ex_e^w = m_w(ex_e^w - ex_0^w) = m_w[h_e^w - h_0^w - T_0(s_e^w - s_0^w)]. \tag{72}$$

Considering that $ex_0^w(p_0, T_0) = 0$, Equation (72) can be expressed as

$$Ex_e^w = m_w(h_e^w - h_0^w)\left(1 - \frac{T_0}{T_{m,0-e}^w}\right) = Q_e^w\left(1 - \frac{T_0}{T_{m,0-e}^w}\right) > 0 \tag{73}$$

because $Q_e^w < 0$ and $\theta_{Q_e}^w = \left(1 - \frac{T_0}{T_{m,0-e}^w}\right) < 0$.

The water leaving HX_3 has a temperature $T_e^w < T_0$ and therefore retains a cooling capacity that can be utilized by other systems.

The exergy of this cooling potential may constitute a useful by-product of the overall system

$$Ex_e^w = \left|Ex_{Q_e}^w\right| = \left|Ex_{Q_R}^w\right| \text{ and} \tag{74}$$

$$Ex_i^w = 0. \tag{75}$$

For the waste-heat stream

$$Ex_e^{WH} = m_g\left[\left(h_e^{WH}(T_{g,e}) - h_0^{WH}(T_0)\right) - T_0\left[\left(s_e^{WH}(T_{g,e}) - s_0^{WH}(T_0)\right]\right] = m_g\left[\left(h_e^{WH}(T_{g,e}) - h_0^{WH}(T_0)\right)\right]\left(1 - \frac{T_0}{T_{m,e-0}^{WH}}\right). \tag{76}$$

Kinetic and potential exergy contributions are neglected for all material streams. For the external waste-heat stream, only the physical-exergy change associated with sensible cooling in HX_4 is included. Chemical exergy is outside the selected system boundary because neither chemical conversion nor the use of the source composition is modeled:

$$Ex_e^{WH} = Ex_{Q_e}^{WH} = \left|Ex_{Q_e}^{WH}\right| = L_{Q_e}^{WH}, \tag{77}$$

given that $m_g\left(h_e^{WH}(T_{g,e}) - h_0^{WH}(T_0)\right) = Q_e^{WH} > 0$ and $1 - \frac{T_0}{T_{m,e-0}^{WH}} = \theta_{Q_e}^{WH} > 0$.

After heat transfer in HX_4, the residual exergy of the waste-heat stream discharged to the environment is treated as a loss. Conversely, the incoming waste-heat stream represents an exergetic input to the discharge stage, and its exergy is evaluated as

$$Ex_i^{WH} = m_g\left[h_i^{WH}(T_{g,i}) - h_0^{WH}(T_0) - T_0\left(s_i^{WH}(T_{g,i}) - s_0^{WH}(T_0)\right)\right] = m_g\left(h_i^{WH}(T_{g,i}) - h_0^{WH}(T_0)\right)\left(1 - \frac{T_0}{T_{m,i-0}^{WH}}\right). \tag{78}$$

Since this incoming stream is cooled in HX_4 while supplying heat to the air stream, its exergy can also be expressed as the exergy of the heat supplied to the system at the temperature level $T_{m,i-0}^{WH}$, i.e., the exergy of the heat released during cooling at constant pressure from $T_{g,i}$ to T_0

$$Ex_i^{WH} = Ex_{Q_i}^{WH} = \left|Ex_{Q_i}^{WH}\right|. \quad (79)$$

The reference source conditions and the nominal 50 K HX_4 design-screening margin are listed in Supplementary Table S1, while Supplementary Table S5 reports the air-side state points of the discharge stage. The source-side heat duty and physical-exergy change are evaluated from the HX_4 energy and exergy balances on the common basis of one kilogram of compressed air for the prescribed turbine inlet temperature T_{11}. The variation in T_{11} therefore provides a steady-state sensitivity to the thermal level available during discharge.

For state 12:

$$Ex_{12} = y[(h_{12} - h_0) - T_0(s_{12} - s_0)] = y(h_{12} - h_0)\left(1 - \frac{T_0}{T_{m,0-12}}\right). \quad (80)$$

By introducing the energy quantity $Q_e^{tur} = y(h_{12} - h_0)$, one gets

$$Ex_{12} = Q_e^{tur}\left(1 - \frac{T_0}{T_{m,0-12}}\right) = Ex_{Q_e}^{tur} = \left|Ex_{Q_e}^{tur}\right| > 0. \quad (81)$$

For state 4′:

$$Ex_{4'} = y[(h_{4'} - h_0) - T_0(s_{4'} - s_0)] = y(h_{4'} - h_0)\left(1 - \frac{T_0}{T_{m,4'-0}}\right) \quad (82)$$

which represents the exergy associated with the refrigeration capacity of the liquefied fraction y, corresponding to the minimum mechanical work required by the Linde–Hampson cryogenic system to produce y kg_{LA}/kg_{CA}:

$$Ex_{4'} = \left|Ex_{Q_f}\right| + C_{min}^{sch}. \quad (83)$$

The mechanical-work terms are associated with the turbine and the cryogenic pump

$$\sum W = W_{tur} + W_P, \quad (84)$$

where in the case of single-stage adiabatic expansion

$$W_{tur} = y(h_{11} - h_{12}), \quad (85)$$

$$W_P = y(h_{4'} - h_9) = -|W_P|. \quad (86)$$

The exergy-destruction terms are associated with the cryogenic pump, the heaters, and the turbine:

$$\sum I = I_P + I_{\Delta T}^{WH} + I_{\Delta T}^{w} + I_{tur} \quad (87)$$

where

$$I_P = yT_0(s_9 - s_{4'}), \quad (88)$$

$$I_{\Delta T}^{w} = T_0[y(s_{10} - s_9) + m_w(s_e^w - s_i^w)], \quad (89)$$

$$I_{\Delta T}^{WH} = T_0\left[y(s_{11} - s_{10}) + m_g\left(s_e^{WH} - s_i^{WH}\right)\right] \text{ and} \quad (90)$$

$$I_{tur} = yT_0(s_{12} - s_{11}). \quad (91)$$

Substituting Equations (71)–(91) into Equation (70) gives:

$$0 = \left|Ex_{Q_R}^{w}\right| + L_{Q_e}^{WH} - \left|Ex_{Q_i}^{WH}\right| + \left|Ex_{Q_e}^{tur}\right| - \left|Ex_{Q_f}\right| - C_{min}^{sch} + W_{tur} - |W_P| + I_P + I_{\Delta T}^{w} + I_{\Delta T}^{WH} + I_{tur}. \quad (92)$$

Rearranging the terms of Equation (92) so that the exergetic fuel of the discharge stage appears on the left-hand side and the product, followed by exergy losses and destruction, appears on the right-hand side, gives

$$\left|Ex_{Q_f}\right| + C_{min}^{sch} + |W_P| + \left|Ex_{Q_i}^{WH}\right| = W_{tur} + \left|Ex_{Q_R}^{w}\right| + \left|Ex_{Q_e}^{tur}\right| + L_{Q_e}^{WH} + I_P + I_{\Delta T}^{w} + I_{\Delta T}^{WH} + I_{tur}. \quad (93)$$

Let Ex_e^{tur} denote the physical exergy remaining in the turbine-exhaust stream. When a suitable external cold sink is available and this exergy is credited, $Ex_{Q_e}^{tur} \equiv Ex_e^{tur}$ is included in the useful product. When no such utilization is credited, $L_{Q_e}^{tur} \equiv Ex_e^{tur}$ is classified as an unrecovered outlet-stream exergy loss. The chilled-water term $Ex_{Q_R}^{w}$ is treated analogously. The practical value of either cooling contribution therefore depends on the availability of an external cooling demand and the extent to which the cooling potential is utilized.

The global liquid air energy storage system consists of two subsystems in series; therefore, the exergetic product of the first subsystem becomes the fuel of the second subsystem ($\left|Ex_{Q_f}\right| + C_{min}^{sch}$).

The recovery-stage turbine and pump formulation was checked against the three-stage adiabatic recovery case reported by Guizzi et al. [30]. The published pressure levels, turbine inlet temperatures, component efficiencies, and mass basis were reproduced, and the resulting deviations in gross turbine work and net recovery work are reported in Supplementary Table S6.

5.2.2. Isothermal Expansion

After analyzing the adiabatic expansion process, the ideal case of isothermal expansion is also investigated to evaluate the maximum work-recovery potential and the exergetic performance of the system.

The conceptual scheme used for the isothermal expansion analysis is shown in Figure 17.

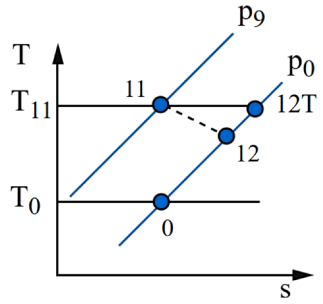


Figure 17. Real and ideal isothermal expansion processes.

The mechanical work of a reversible isothermal expansion at temperature T_{11} is:

$$W_{tur}^{T_{11}} = y[T_{11}(s_{12T} - s_{11}) - (h_{12T} - h_{11})]. \quad (94)$$

The physical exergy carried by the outlet air stream at state 12T is given by

$$Ex_{12T} = y[(h_{12T} - h_0) - T_0(s_{12T} - s_0)] = y(h_{12T} - h_0)\left(1 - \frac{T_0}{T_{m,0-12T}}\right). \quad (95)$$

Since $p_{12T} = p_0$, this quantity represents the thermal component of the outlet-stream physical exergy. When it is not recovered, it is treated as the outlet-stream exergy loss $Ex_{12T} = L_{Q_e,tur}^{T_{11}}$. Then, the exergy balance takes the form

$$\left|Ex_{Q_f}\right| + C_{min}^{sch} + |W_P| + \left|Ex_{Q_i}^{WH}\right| = W_{tur,air}^{iso} + \left|Ex_{Q_R}^{w}\right| + L_{Q_e,tur}^{T_{11}} + L_{Q_e}^{WH} + I_P + I_{\Delta T}^{w} + I_{\Delta T}^{WH}, \quad (96)$$

where $W^{iso}_{tur,air}$ denotes the decrease in the physical exergy of the air stream during reversible isothermal expansion at T_{11}.

During reversible isothermal expansion, heat is supplied continuously to maintain the working fluid at T_{11}, according to the entropy balance:

$$Q^{T_{11}} = y \cdot T_{11}(s_{12T} - s_{11}). \tag{97}$$

The corresponding exergy input is

$$Ex_Q^{T_{11}} = Q^{T_{11}}\left(1 - \frac{T_0}{T_{11}}\right). \tag{98}$$

For a real gas, enthalpy may vary with pressure even at constant temperature; therefore, the heat supplied during the isothermal process is not generally equal to the turbine work. The turbine work is evaluated from the real-gas enthalpy and entropy values according to Equation (94).

During reversible isothermal expansion, continuous heat addition maintains the working fluid at T_{11} and contributes to the mechanical work produced. If $T_{11} = T_0$, this heat can be supplied by the environment with zero associated exergy transfer. At $T_{11} > T_0$, the supplied heat carries exergy and forms part of the exergetic fuel of the discharge stage. The turbine work then comprises a contribution from this thermal-exergy input and a contribution associated with the decrease in the physical exergy of the air stream.

The contribution associated with the decrease in the physical exergy of the air stream is written as

$$W^{iso}_{tur,air} = W^{T_{11}}_{tur} - \left|Ex_Q^{T_{11}}\right| = y[T_0(s_{12T} - s_{11}) - (h_{12T} - h_{11})]. \tag{99}$$

Equation (99) represents the contribution to turbine work associated with the decrease in flow exergy between states 11 and 12T. The outlet stream retains the physical exergy Ex_{12T}, which is included in the balance as an unrecovered outlet-stream loss when no external cold sink is credited.

At $T_{11} = T_0$, the exergy associated with the supplied heat is zero. If the outlet also reaches the environmental state, $p_{12T} = p_0$ and $T_{12T} = T_0$, the outlet-stream exergy becomes zero and the reversible turbine work is determined entirely by the inlet-stream exergy. For $T_{11} > T_0$, the supplied thermal exergy also contributes to the work produced.

Accordingly, the exergy balance includes $W^{T_{11}}_{tur,u}$ as the mechanical-work output and $Ex_Q^{T_{11}}$ as a thermal-exergy input. The ideal isothermal case therefore provides an upper thermodynamic benchmark for work recovery under continuous heat addition.

The isothermal limit can be approached technically by increasing the number of adiabatic expansion stages with intermediate reheating. Exact isothermal expansion corresponds to the idealized limiting case of infinitely many stages with infinitesimal temperature changes and continuous heat addition. Finite heat-transfer area, non-zero temperature differences, pressure losses, and practical staging constraints prevent this limit from being attained in real equipment. The two-stage configuration is therefore retained as a technically feasible intermediate architecture.

Substituting Equation (99) into Equation (96) gives

$$\left|Ex_{Q_f}\right| + C^{sch}_{min} + |W_P| + \left|Ex^{WH}_{Q_i}\right| + \left|Ex_Q^{T_{11}}\right| = W^{T_{11}}_{tur} + \left|Ex^{w}_{Q_R}\right| + L^{T_{11}}_{Q_e,tur} + L^{WH}_{Q_e} + I_P + I^{w}_{\Delta T} + I^{WH}_{\Delta T}. \tag{100}$$

The following exergetic considerations apply to adiabatic and isothermal turbine expansion:

(a) For isothermal expansion, $W^{T_{11}}_{tur} > W^{\delta Q=0}_{tur}$. When the expansion is performed at $T_{11} > T_0$, the exergy associated with the heat supplied to maintain the isothermal

process constitutes part of the exergetic fuel. Conversely, for isothermal expansion at the environmental temperature ($T_{11} = T_0$), the exergy of the supplied heat is zero, although the heat input remains essential for maintaining the isothermal process.

(b) In the case of adiabatic expansion, if the cooling effect is considered a useful product, its exergy should be accounted for together with the turbine work, $W_{tur}^{\delta Q=0}$. Accordingly, the overall exergetic performance coefficient should include the exergy associated with this additional useful product.

5.3. Study of the Influence of Cryogenic Pumping Pressure and Turbine Inlet Temperature

This analysis focuses on the energy recovery stage (ERS), in which part of the energy stored in the liquefied air produced during the liquefaction process is recovered through adiabatic expansion in a single-stage turbine. The design parameters considered were the cryogenic pumping pressure p_9 and the turbine inlet temperature T_{11}. The results were analyzed through stage exergetic efficiency and through the shares of the main exergy destruction or losses, referred to the stage fuel exergy.

5.3.1. The Influence of Cryogenic Pumping Pressure

The discharge-stage output comprises the mechanical work developed by the turbine and, when suitable external sinks are available, two recoverable cooling contributions: the cold exergy of the turbine exhaust and the cooling potential associated with water cooled from 300 K to 280 K in HX_3. All quantities are reported per kilogram of compressed air. Because no cooling-demand profile or sink-utilization factor is modeled, the two cooling terms are treated as recoverable potentials rather than as guaranteed delivered products.

A minimum terminal temperature difference of 10 K was imposed in HX_3, whereas 50 K was adopted as a nominal design-screening margin for HX_4 [31]. Segmented temperature–enthalpy verification over the investigated p_9 range identified no internal temperature crossover; the corresponding results are reported in Supplementary Table S9.

Under these conditions, the discharge stage can be interpreted as an energy recovery unit with simultaneous production of mechanical work and cooling effect.

Considering the exergy balance for the discharge stage with single-stage adiabatic expansion, as expressed by Equation (93), the product and fuel of the stage are given by

$$P_{tot} = W_{tur} + \left|Ex_{Q_R}^{w}\right| + \left|Ex_{Q_e}^{tur}\right|, \tag{101}$$

$$F_{dis} = \left|Ex_{Q_f}\right| + C_{min}^{sch} + |W_P| + \left|Ex_{Q_i}^{WH}\right|. \tag{102}$$

Thus, the exergetic efficiency can be written as

$$\eta_{ex} = \frac{P_{tot}}{F_{dis}}. \tag{103}$$

The variation in exergetic efficiency and of the exergy-destruction shares with pumping pressure p_9 is shown in Figure 18.

Figure 18 shows that increasing the cryogenic pumping pressure p_9 in the range 8–20 MPa leads to a significant increase in the exergetic efficiency of the discharge stage, from 39.29% to 43.93%. Most of this improvement occurs up to approximately 16 MPa, where the efficiency reaches 42.93%. Above this value, the gain becomes smaller, with the efficiency increasing by only 1.00 percentage point between 16 MPa and 20 MPa. Therefore, a pressure of approximately 16 MPa can be retained as a representative value for the continuation of the analysis, since it provides most of the performance improvement without imposing the highest pumping pressure.

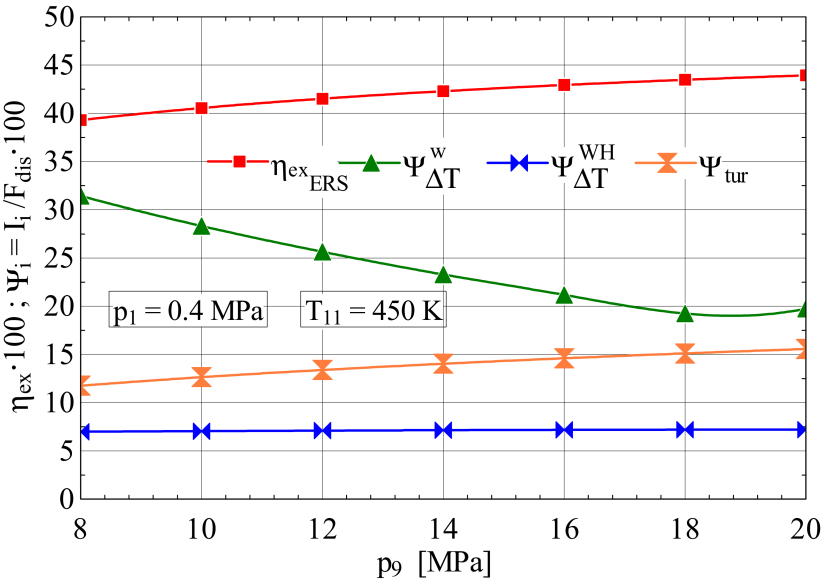


Figure 18. Variation in exergetic efficiency and exergy-destruction shares Ψ_i in system components with the cryogenic pumping pressure p_9.

The increase in exergetic efficiency is mainly associated with the reduction in the exergy-destruction share in the first heater, HX_3, where liquid air is regasified by the water stream. The contribution $\Psi^{w}_{\Delta T}$ decreases from 31.44% at $p_9 = 8$ MPa to 21.17% at $p_9 = 16$ MPa and reaches 19.75% at $p_9 = 20$ MPa. The minimum value in the analyzed range is obtained around 18 MPa, where $\Psi^{w}_{\Delta T} = 19.24\%$. In contrast, the turbine irreversibility share increases from 11.75% to 15.57%, because the expansion ratio and the available turbine work increase with the pumping pressure. The exergy-destruction share in the waste-heat heater, $\Psi^{WH}_{\Delta T}$, remains almost unchanged, varying only from 6.987% to 7.212%, while the exergy loss associated with the discharged waste-heat stream decreases slightly from 6.150% to 5.315%.

The decrease in exergy destruction in the first heater is not caused by a significant change in the air temperature after pumping. In the analyzed range, at supercritical pressures, the temperature of state 9 remains in a narrow cryogenic range (from 98.75 K to 104.2 K), whereas the temperature of state 10 is imposed at 290 K by the water-heater outlet condition. Therefore, the reduction in irreversibility is mainly related to the decrease in the heat duty of HX_3. Consequently, the exergy destruction in HX_3 decreases from approximately 39.4 to 25.3 kJ/kg$_{CA}$. The slight increase in $\Psi^{w}_{\Delta T}$ between 18 MPa and 20 MPa suggests that the benefit of further pressure increases gradually diminishes, as the real-fluid thermodynamic properties of high-pressure cryogenic air begin to limit additional reductions in heat-transfer irreversibility.

Figure 19 presents the energy recovery-stage products as a function of p_9.

The useful products of the discharge-stage increase with the pumping pressure p_9 (Figure 19). The total product P_{tot} increases by approximately 14.36%, reaching 56.32 kJ/kg$_{CA}$. The mechanical work developed in the turbine, W_{tur}, increases moderately from 41.691 to 45.360 kJ/kg$_{CA}$, i.e., by about 8.8%, while the cold exergy associated with the air stream discharged from the turbine, $Ex^{tur}_{Q_R}$ increases more significantly, from 5.652 to 9.246 kJ/kg$_{CA}$, corresponding to an increase of approximately 63.59%. In contrast, the exergy associated with the chilled water product, $Ex^{w}_{Q_R}$ remains almost constant, showing a slight decrease from 1.908 to 1.715 kJ/kg$_{CA}$, because the heat duty transferred in HX_3 decreases as the pumping pressure increases.

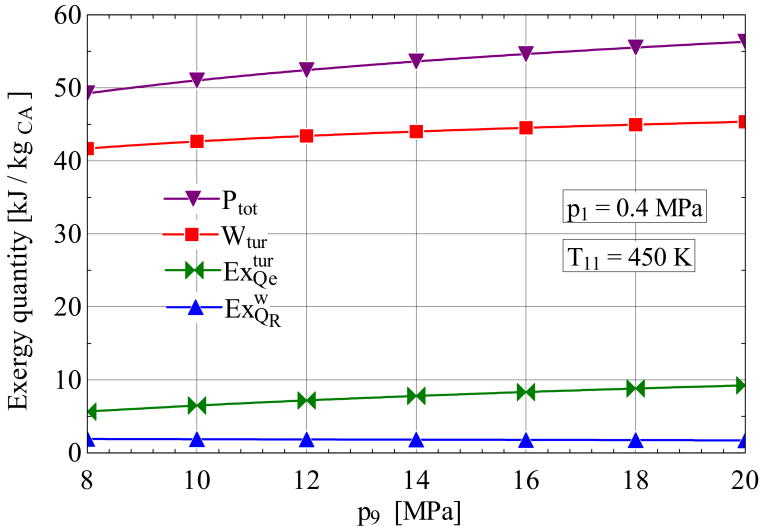


Figure 19. Variation in the energy recovery stage products as a function of pumping pressure p_9.

Figure 20 compares the structural liquefaction exergetic indicator, $\eta_{ex_{Linde}}$, the exergetic efficiency of the energy recovery stage, $\eta_{ex_{ERS}}$, and the global exergetic efficiency, $\eta_{ex_{global}}$, as functions of p_9.

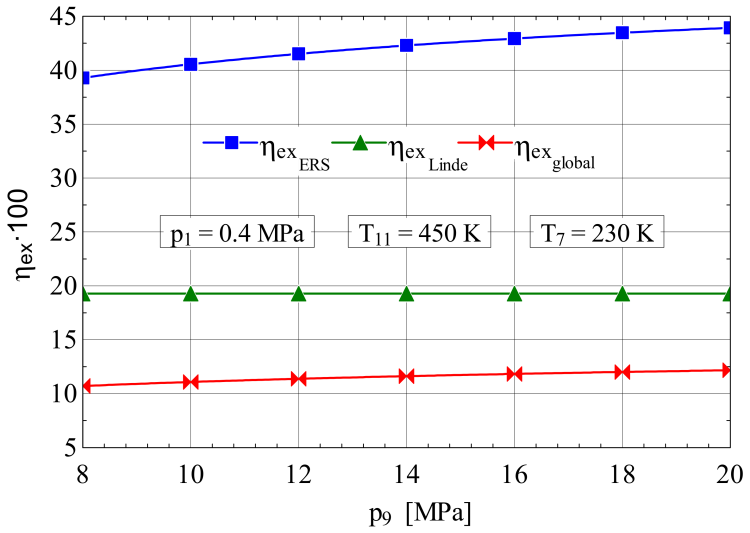


Figure 20. Exergetic performance indicators as a function of pumping pressure p_9.

In the system efficiency diagram (Figure 20), the efficiency of the energy recovery stage increases from 39.29% to 43.93% as p_9 increases, while the efficiency of the Linde–Hampson liquefaction stage remains constant at 19.28% because it is not affected by the changes imposed in the recovery stage. The global exergetic efficiency of the modeled system shows a relative increase of approximately 13.63%, much smaller than the increase in the efficiency of the discharge stage. The principal limitation of the global system therefore lies in the liquefaction stage, whose performance is lower than that of the recovery stage.

5.3.2. The Influence of Turbine Inlet Temperature

The influence of the air temperature at the turbine inlet T_{11} was analyzed for the adopted pumping pressure $p_9 = 16$ MPa. This parameter controls both the mechanical work recovered in the turbine and the utilization of the external waste-heat stream. Within the adopted HX_4 design-screening framework, varying T_{11} provides a steady-state assessment of the air-side heating level attainable from the external thermal stream.

Increasing the turbine inlet temperature T_{11} has a more pronounced influence on the performance of the discharge stage than varying the pressure. Thus, over the range T_{11} = 350–600 K, the exergetic efficiency increases from 39.80% to 51.30%, and the 50% threshold is exceeded for T_{11} values between 550 K and 600 K (Figure 21). The main cause of the increase in efficiency is the rapid reduction in the exergy loss associated with the residual physical exergy of the waste-heat stream leaving HX_4. The share $\Psi_{L_{Qe}^{WH}}$ decreases sharply, from 11.86% to 0.175%, as T_{11} increases from 350 K to 600 K. In other words, increasing the turbine inlet air temperature uses the available physical exergy of the waste-heat stream more effectively, and the amount of unused discharged exergy becomes much smaller.

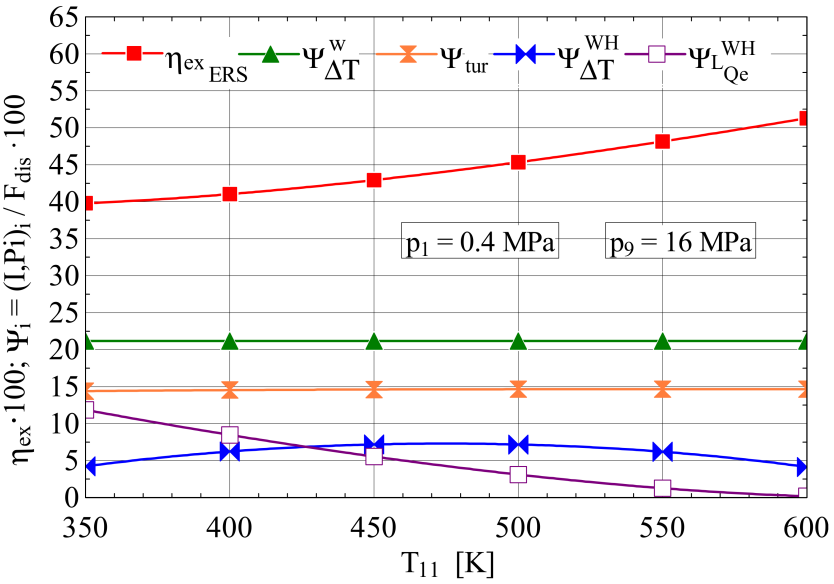


Figure 21. Variation in exergetic efficiency and exergy-destruction shares Ψ_i in system components with the air temperature T_{11} at the turbine inlet.

The share $\Psi^{w}_{\Delta T}$ remains almost constant, because the first heat exchanger is not directly affected by the change in T_{11}. The share Ψ_{tur} also remains almost constant, with only a minor increase from 14.38% to 14.64%. The share of exergy destruction associated with the finite temperature difference in the waste-heat exchanger HX_4, $\Psi^{WH}_{\Delta T}$, has a non-uniform evolution: it increases from 4.216% to 7.18% up to approximately T_{11} = 450 K, then decreases to 4.133% for T_{11} = 600 K. This behavior is explained by the fact that exergy destruction in the heat exchanger depends simultaneously on the heat duty and on the finite temperature difference. Initially, the increase in heat duty dominates and irreversibility increases; subsequently, the convergence of temperature levels becomes more important and irreversibility decreases.

The cryogenic pump irreversibility is not affected by T_{11} in this analysis, because the pumping pressure is kept constant at 16 MPa. Its normalized contribution remains approximately 8.57% and is therefore not responsible for the trends observed in this section.

Over the investigated T_{11} range, no internal temperature crossover was identified. At T_{11} = 600 K, the minimum local temperature difference in HX_4 decreased to 41.41 K; although it remained positive, this endpoint does not satisfy the nominal 50 K screening margin and is retained in Figures 21–23 only as a thermodynamic upper bound (Supplementary Table S9).

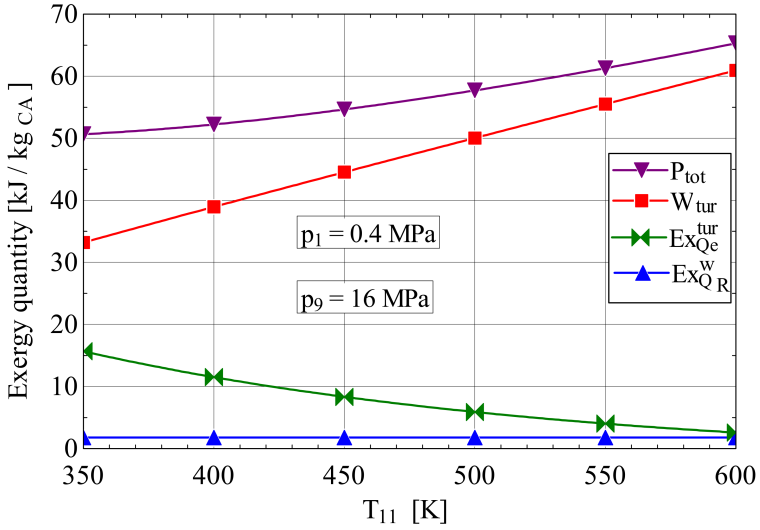


Figure 22. Variation in the energy recovery stage products with turbine inlet temperature T_{11}.

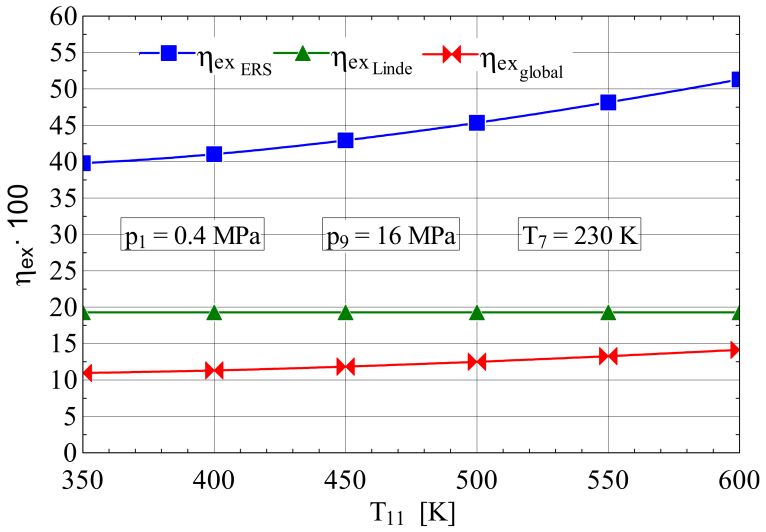


Figure 23. Exergetic performance indicators as a function of turbine inlet temperature T_{11}.

Increasing temperature T_{11} significantly changes the structure of the discharge-stage product (Figure 22). The total useful product P_{tot} increases from 50.647 to 65.291 kJ/kg$_{CA}$, the dominant component being the turbine work W_{tur}, which increases significantly from 33.195 to 60.938 kJ/kg$_{CA}$. This evolution is explained by the fact that the air enters the turbine with higher enthalpy, which increases the capacity to produce mechanical work during expansion.

In parallel, the cold exergy of the air stream at the turbine outlet $\left|Ex_{Qe}^{tur}\right|$ decreases considerably, from 15.679 to 2.581 kJ/kg$_{CA}$. This reduction occurs because a higher inlet temperature also leads, under expansion conditions, to a higher outlet temperature, thereby reducing the cooling potential of the exhaust gas. The exergy of chilled water remains practically constant, around 1.772 kJ/kg$_{CA}$, because this component of the plant is not significantly affected by the variation in T_{11}.

In the system efficiency diagram (Figure 23), increasing T_{11} increases the efficiency of the discharge stage and, consequently, the global exergetic efficiency, from 10.97% to 14.14%. However, the global exergetic efficiency remains much lower than the efficiency of the recovery stage because of the low structural liquefaction exergetic indicator of the Linde–Hampson cycle. Therefore, improving global performance cannot be achieved by

improving the discharge stage alone; improvement in the liquefaction stage or the selection of a more advantageous expansion architecture is also required.

5.4. Comparative Analysis

In the energy recovery stage of a liquid air storage system, the expansion process plays an essential role in determining the mechanical work that can subsequently be converted into electricity. In the case of single-stage adiabatic expansion, the air temperature decreases significantly, leading both to mechanical-work production and to the appearance of a residual cold resource. However, from a thermodynamic point of view, the mechanical work produced by the turbine can be increased if the expansion process is staged, thereby approaching an isothermal evolution.

Because of this, the comparative analysis is extended beyond the single-stage adiabatic configuration. Three expansion strategies are compared: single-stage adiabatic expansion, two-stage adiabatic expansion with intermediate reheating, and ideal isothermal expansion. The analysis is performed for the reference regime characterized by $p_0 = 0.1\text{MPa}$, $p_1 = 0.4\text{MPa}$, $T_{11} = 550\ \text{K}$ and $p_9 = 16\text{MPa}$, previously established as representative for the analyzed LAES configuration (Linde–Hampson liquefaction cycle, with external auxiliary pre-cooling and two recuperative heat exchangers).

For the discharge stage, the specific turbine work recovered per kilogram of liquid air is defined as

$$w_{0,tur} = \frac{W_{tur}}{y}\left[\frac{MJ}{kg_{LA}}\right]. \tag{104}$$

The liquefaction stage is characterized by the net-specific mechanical-work input per kilogram of liquid air:

$$w_0 = \frac{\left|W_{liq}\right|}{y}\left[\frac{MJ}{kg_{LA}}\right]. \tag{105}$$

The recovery factor of the mechanical energy consumed in the liquefaction block is

$$RF = \frac{w_{0,tur}}{w_0} = \frac{W_{tur}}{\left|W_{liq}\right|}, \tag{106}$$

and the exergetic recovery factor is

$$ExRF = \frac{P_{tot}}{\left|W_{liq}\right|}. \tag{107}$$

The mechanical-energy recovery factor RF provides a work-recovery indicator without assigning credit to the cooling products, whereas ExRF includes the total useful exergetic product recovered during discharge. Both quantities are recovery factors referenced to the mechanical input of the liquefaction block and do not represent complete electrical storage-cycle performance indicators.

The liquefaction and energy recovery blocks are connected in series. The exergy carried by the stored liquid air,

$$Ex_{LA} = Ex_{Q_f} + C^{sch}_{min}, \tag{108}$$

is the product of the liquefaction block and an internal fuel of the discharge block. It must therefore be excluded from the external fuel of the coupled system to avoid double counting. Let F_{dis} denote the total exergetic fuel of the discharge stage. The global exergetic efficiency of the modeled liquefaction–recovery chain is defined as

$$\eta_{ex,global} = \frac{P_{tot}}{W_{liq} + F_{dis} - Ex_{LA}} = \begin{cases} \dfrac{W_{tur} + Ex^{w}_{Q_R} + Ex^{tur}_{Q_e}}{W_{liq} + W_P + Ex^{WH}_{Q_i}}, \text{one stage adiabatic expansion} \\ \dfrac{W_{tur} + Ex^{w}_{Q_R} + Ex^{tur}_{Q_e}}{W_{liq} + W_P + \sum_{k=1}^{2}\left(Ex^{WH}_{Q_i}\right)_k}, \text{two stage adiabatic expansion} \\ \dfrac{W_{tur} + Ex^{w}_{Q_R}}{W_{liq} + W_P + Ex^{WH}_{Q_i} + Ex^{T_{11}}_{Q}}, \text{ideal isothermal expansion} \end{cases}, \quad (109)$$

where W_{liq} is the total external mechanical input to the liquefaction block, including the auxiliary refrigeration input where applicable. The inlet water stream is at the environmental state and therefore has zero inlet exergy. The useful-product components and the resulting global exergetic efficiencies are reported in Table 1 and illustrated in Figure 24b. The turbine-exhaust cold exergy is included as a recoverable product only for the adiabatic cases; in the ideal isothermal case, the residual outlet-stream exergy is treated as a loss. For the reference Linde–Hampson case with two-stage adiabatic expansion, $W_{liq} = 436.842\ kJ/kg_{CA}$, $F_{dis} = 148.411\ kJ/kg_{CA}$, $Ex_{Q_f} = 84.228\ kJ/kg_{CA}$ and $C^{sch}_{min} = 18.212\ kJ/kg_{CA}$. The cryogenic pump input is $W_P = 3.695\ kJ/kg_{CA}$, while the total physical-exergy input supplied by the two external thermal streams is $\sum_{k=1}^{2}(Ex^{WH}_{Q_i})_k = 42.276\ kJ/kg_{CA}$. Thus, with $P_{tot} = 76.840\ kJ/kg_{CA}$, Equation (109) gives $\eta_{ex,global} = 15.92\%$. This value corresponds to the aggregated compressor representation adopted in the main parametric model; the corresponding finite-stage compressor sensitivity is reported in Supplementary Table S12.

Equation (109) corresponds to the multi-product interpretation, in which the available cooling contributions are fully credited. To quantify the influence of cooling utilization, a work-only global exergetic efficiency is also defined by retaining only the turbine work in the useful product:

$$\eta^{W}_{ex,global} = \frac{W_{tur}}{W_{liq} + F_{dis} - Ex_{LA}} \quad (110)$$

For two-stage expansion, W_{tur} denotes the sum of the work produced by the two turbines. The denominator is unchanged from Equation (109), so all external mechanical and thermal-exergy inputs remain included. Accordingly, $\eta^{W}_{ex,global}$ remains a work-only exergetic indicator of the modeled liquefaction–recovery chain; it retains the external thermal-exergy input and excludes storage-duration and electrical-conversion effects. Equations (109) and (110) therefore represent the limiting cases of full and zero utilization of the recoverable cooling potentials, respectively. Partial utilization would produce an intermediate global exergetic efficiency.

The global exergetic efficiency $\eta_{ex,global}$ of the modeled liquefaction–recovery chain is strongly limited by the performance of the Linde–Hampson liquefaction block. The analysis is therefore extended by considering the selected Claude–Heylandt reference liquefaction block from Ref. [17] to evaluate the influence of liquefaction technology under the same discharge-stage assumptions.

To compare the two liquefaction configurations, Table 1 presents the energy and exergy quantities and the associated performance indicators of the LAES system based on the Linde–Hampson and Claude–Heylandt cycles.

The model-specific assumptions, expander flow split, net liquefaction work, and principal state points of the selected Claude–Heylandt reference block are reported in Supplementary Tables S10 and S11, respectively.

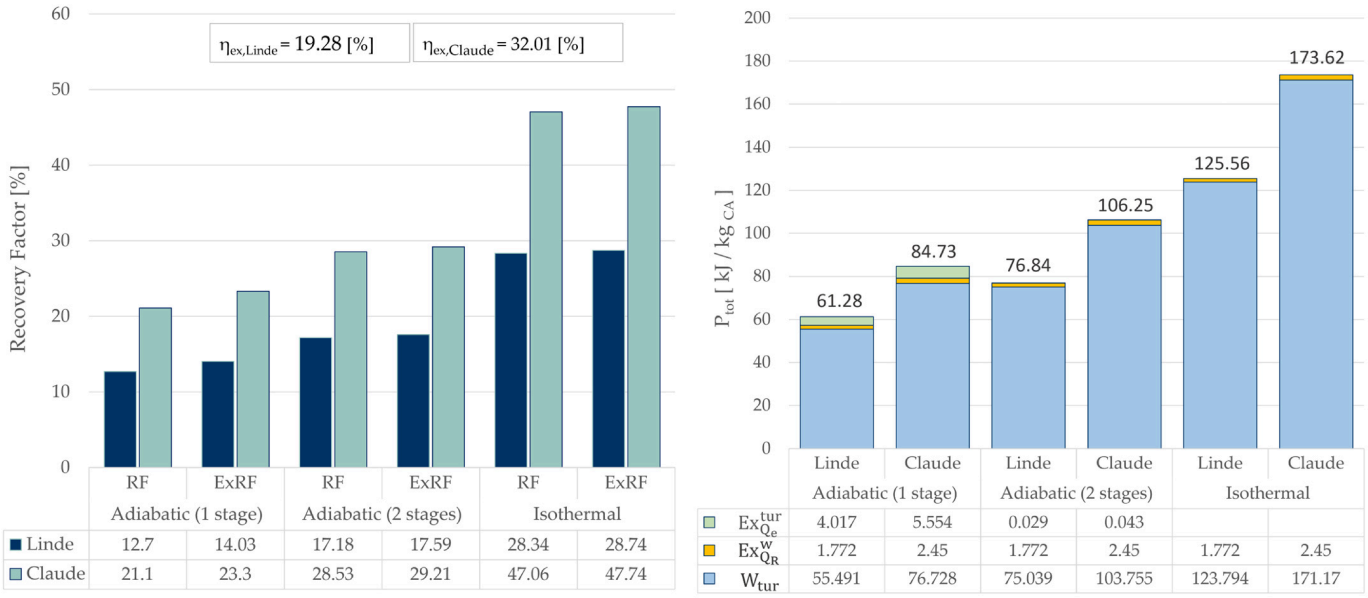
Table 1. Discharge-stage energy and exergy quantities per kilogram of compressed air and performance indicators of the Linde–Hampson- and Claude–Heylandt-based LAES systems.

Cycle	Linde–Hampson			Claude–Heylandt *		
Parameter \ Expansion	Adiabatic (1 Stage)	Adiabatic (2 Stages)	Isothermal (Ideal)	Adiabatic (1 Stage)	Adiabatic (2 Stages)	Isothermal (Ideal)
$\eta_{ex_{ERS}}$ [%]	48.15	51.78	68.41	48.15	51.78	68.41
η_{ex} [%] (structural liquefaction exergetic indicator)	19.28	19.28	19.28	32.01	32.01	32.01
$\eta_{ex_{global}}$ [%]	13.27	15.92	24.24	21.29	24.87	36.48
$\eta^{W}_{ex_{global}}$ [%]	12.02	15.54	23.90	19.28	24.28	35.97
$\Psi^{w}_{\Delta T}$ [%]	21.17	18.16	14.68	21.17	18.16	14.68
$\Psi^{WH}_{\Delta T}$ [%]	6.19	9.92	4.29	6.19	9.92	4.29
Ψ_{tur} [%]	14.65	9.30	–	14.65	9.30	–
$w_0 \left[\frac{MJ}{kg_{LA}}\right]$ (net-specific liquefaction work)	2.862	2.862	2.862	1.724	1.724	1.724
$w_{0,tur} \left[\frac{MJ}{kg_{LA}}\right]$ (recovered turbine work)	0.364	0.492	0.811	0.364	0.492	0.811
RF [%]	12.70	17.18	28.34	21.10	28.53	47.06
P_{tot} [kJ/kg$_{CA}$]	61.280	76.840	125.566	84.732	106.247	173.62
W_{tur} [kJ/kg$_{CA}$]	55.491	75.039	123.794	76.728	103.755	171.17
$Ex^{tur}_{Q_e}$ [kJ/kg$_{CA}$]	4.017	0.029	–	5.554	0.043	–
$Ex^{w}_{Q_R}$ [kJ/kg$_{CA}$]	1.772	1.772	1.772	2.45	2.45	2.45
ExRF [%]	14.03	17.59	28.74	23.3	29.21	47.74

Notes: All absolute quantities are reported per kilogram of compressed air, whereas w_0 and $w_{0,tur}$ are reported per kilogram of liquid air. * The Claude–Heylandt block was recalculated using the same reference environment, storage pressure, upper pressure, AIR_ha real-fluid property model, heat-ingress assumptions, product–fuel definitions, and mass basis as the improved Linde–Hampson block. P_{tot} includes turbine work and the recoverable cooling terms shown separately in the table. The work-only indicator $\eta^{W}_{ex,global}$ retains the same external fuel terms but credits only turbine work. The multi-product and work-only indicators represent the upper- and lower-utilization bounds for cooling credit, respectively. Storage-duration-dependent losses and electrical-conversion efficiencies are outside the system boundary.

For a given expansion architecture, the same discharge-stage model and component efficiencies are applied to both liquefaction blocks. Consequently, the normalized discharge-stage efficiency and destruction shares are identical, whereas the absolute products per kilogram of compressed air are higher for the Claude–Heylandt case because it produces a larger liquid fraction.

Table 1 shows that the Claude–Heylandt liquefaction configuration improves the global recovery performance for all expansion strategies analyzed. Although the behavior of the discharge stage remains similar, the higher efficiency of the liquefaction process and the lower specific mechanical-work consumption in the Claude–Heylandt cycle lead to higher values of both the mechanical-energy recovery factor RF and the exergetic recovery factor ExRF (Figure 24a). The highest recovery level is obtained for the ideal isothermal expansion case, for which the mechanical contribution becomes dominant within the total recovery factor.



(**a**) (**b**)

Figure 24. Comparison of the energy and exergy performance of the Linde–Hampson and Claude–Heylandt liquefaction configurations as a function of the expansion strategy: (**a**) variation in the mechanical-energy recovery factor RF and of the total exergetic recovery factor ExRF; (**b**) decomposition of the multi-product exergy output P_{tot} into turbine work and recoverable cooling contributions.

Figure 24b shows that the useful exergetic product P_{tot} increases when moving from single-stage adiabatic expansion to two-stage expansion and then to ideal isothermal expansion. In all cases, the dominant contribution is turbine work W_{tur}, while the recoverable cold exergy contributions are significantly lower. This indicates that the performance improvement is primarily associated with increased mechanical-work recovery rather than with the recoverable cold exergy component.

Excluding both recoverable cooling terms decreases the global exergetic efficiency by 0.34–1.25 percentage points for the Linde–Hampson cases and by 0.51–2.01 percentage points for the Claude–Heylandt cases. The largest difference occurs for single-stage adiabatic expansion because this configuration retains the greatest turbine-exhaust cooling potential. The exclusion of cooling credit does not change the relative ranking of the liquefaction cycles or expansion architectures.

6. Conclusions

This paper presents a sustainability-oriented comparative and parametric exergetic analysis of LAES systems, integrating liquefaction and discharge within a unified product–fuel framework. The principal contribution is the separation of the useful cryogenic product, scheme-imposed minimum thermodynamic consumption, exergy destruction, and exergy losses. This structural interpretation links cycle architecture and operating parameters to thermodynamic resource degradation, mechanical-work recovery, and recoverable cooling potential.

The results identify the liquefaction process as the primary limitation of overall LAES performance. In the basic Linde–Hampson cycle, the throttling valve and recuperative heat exchanger are the dominant sources of exergy destruction, and operating parameters cannot be selected solely based on the liquefied air fraction or specific energy consumption. External auxiliary pre-cooling improves performance by reducing throttling irreversibilities; however, it may introduce recoverable losses if the cold potential of the return stream is

not internally recovered. Among the analyzed configurations, the Linde–Hampson system with two recuperative heat exchangers and intermediate auxiliary pre-cooling achieves the best performance, improving temperature matching and internal cold recovery. Under the investigated conditions, the structural liquefaction exergetic indicator increases from 7.95% for the basic configuration to 19.28% for the improved configuration. A subsequent equipment-level design should complement this result by considering heat-exchanger area, pressure-drop penalties, auxiliary refrigeration requirements, and cost.

The discharge-stage analysis highlights the influence of cryogenic pumping pressure, turbine inlet temperature, and expansion architecture on the useful system output. A pumping pressure of approximately 16 MPa is identified as an appropriate operating level, beyond which efficiency gains become marginal under the assumptions of the present model. The turbine inlet temperature has a stronger influence on the discharge process. Within the range satisfying the adopted HX_4 screening criterion, a higher T_{11} increases the air enthalpy available for expansion, raises the mechanical work produced by the turbine, and improves the utilization of the external thermal stream. At the same time, the higher turbine-exhaust temperature reduces the residual cold exergy available at the outlet, revealing a trade-off between mechanical-work recovery and recoverable cooling potential. No single operating condition is preferable for every application: a system intended primarily for work recovery would generally favor a higher turbine inlet temperature, whereas an application with access to a suitable cold sink may accept a lower work output in exchange for a greater cooling potential. The operating conditions and expansion architecture should consequently be selected according to the relative importance assigned to these two products.

The comparison between single-stage adiabatic expansion, two-stage adiabatic expansion with reheating, and ideal isothermal expansion demonstrates the strong influence of expansion architecture on recovery performance. Ideal isothermal expansion yields the maximum mechanical work and the highest exergetic efficiency of the discharge stage (68.41%), but it should be regarded as an upper thermodynamic benchmark rather than a practically realizable configuration. In contrast, adiabatic expansion, particularly in a two-stage arrangement with reheating, is more suitable for multi-energy applications, as it provides turbine work together with recoverable cooling potential. For the representative two-stage adiabatic case evaluated with the aggregated compressor representation adopted for the main parametric analysis, the global exergetic efficiency of the modeled liquefaction–recovery chain reaches 15.92% for the improved Linde–Hampson configuration and increases to 24.87% for the selected Claude–Heylandt reference block. Under the common discharge-stage assumptions adopted in this study, this controlled comparison highlights the strong influence of the liquefaction block on overall LAES performance. The same configuration ranking is obtained when the recoverable cooling contributions are excluded and only turbine work is credited as the useful product.

Taken together, the results support viewing LAES as more than an electricity-storage unit. In the configurations examined here, the discharge stage connects the stored cryogenic resource with mechanical-work recovery, the utilization of the physical exergy of an available external thermal stream, and, when suitable external sinks are present, recoverable cooling potential. This broader system perspective provides the basis for the sustainability-oriented interpretation adopted in the study. At the same time, that interpretation remains deliberately thermodynamic: the present analysis addresses resource efficiency, exergy destruction and losses, external-heat utilization, and the recovery of useful exergetic outputs, but it does not establish economic feasibility, environmental benefit, reductions in carbon emissions, or life-cycle performance.

The operating points and efficiencies reported in this study should therefore be interpreted as reference thermodynamic results for the adopted steady-state conditions, common mass basis, and idealized component assumptions. The combined cases presented in Supplementary Table S8 show how simultaneous changes in the principal assumptions can shift the absolute system performance, but they represent deterministic bounds rather than statistical confidence intervals. A complete engineering assessment would also require dynamic and partial-load operation, storage-duration effects, pressure drops, component sizing, and a detailed representation of the interaction with real renewable-generation profiles and industrial thermal sources. These technical extensions should be accompanied by techno-economic and environmental analyses. Extending the present framework in these directions would make it possible to determine not only which configuration is thermodynamically preferable, but also under what practical conditions it becomes technically, economically, and environmentally viable.

Supplementary Materials: The following supporting information can be downloaded at: https://www.mdpi.com/article/10.3390/su18168605/s1, Table S1: Summary of the principal operating conditions, component performance assumptions, and boundary conditions used in the simulations; Table S2: Representative state-point table for the baseline Linde–Hampson liquefaction cycle; Table S3: Representative state-point table for the Linde–Hampson cycle with external auxiliary pre-cooling; Table S4: Representative state-point table for the Linde–Hampson cycle with two recuperative heat exchangers and intermediate auxiliary pre-cooling; Table S5: Thermodynamic properties at representative state points for the single-stage adiabatic discharge expansion case; Table S6: Literature consistency comparison for the EES liquefaction models and quantitative check of the recovery-stage turbine submodel [14,30,32]; Table S7: One-factor sensitivity analysis of secondary model assumptions for the improved Linde–Hampson configuration; Table S8: Combined deterministic robustness envelope for the improved Linde–Hampson configuration coupled with two-stage adiabatic expansion; Table S9: Segmented temperature–enthalpy verification of minimum local temperature differences over the complete investigated parametric ranges; Table S10: Model-specific assumptions and key liquefaction results for the Claude–Heylandt liquefaction block [17]; Table S11: Principal state points for the Claude–Heylandt liquefaction block [17]; Table S12: Comparison of the aggregated isothermal-efficiency and finite-stage intercooled compressor models for the three reference Linde–Hampson configurations.

Author Contributions: Conceptualization, A.A.P., A.D. and L.G.; methodology, A.D., L.G. and D.C.U.; software, A.D. and A.A.P.; validation, D.C.U. and L.G.; formal analysis, A.A.P., D.C.U. and A.D.; investigation, D.C.U. and L.G.; resources, A.D. and A.A.P.; data curation, L.G.; writing—original draft preparation, A.A.P. and A.D.; writing—review and editing, A.A.P. and A.D.; visualization, A.A.P. and D.C.U.; supervision, L.G. and A.D.; project administration, A.A.P. and A.D.; funding acquisition, A.D. All authors have read and agreed to the published version of the manuscript.

Funding: This research received no external funding.

Institutional Review Board Statement: Not applicable.

Informed Consent Statement: Not applicable.

Data Availability Statement: The thermodynamic assumptions, representative state points, literature benchmark comparisons, and sensitivity results reported in this study are provided in the article and Supplementary Materials.

Conflicts of Interest: The authors declare no conflicts of interest.

Nomenclature

The following symbols and abbreviations are used in this manuscript:

Abbreviations	
CA	compressed air
COP	coefficient of performance
CP	compressor
EES	Engineering Equation Solver
ERS	energy recovery stage
EV	evaporator
HX	heat exchanger
LA	liquid air
LAES	liquid air energy storage
LAST	liquid air storage tank
LNG	liquefied natural gas
LS	liquid separator
ORC	Organic Rankine Cycle
P	cryogenic liquid pump
RHX	recuperative heat exchanger
TV	throttling valve
WH	external waste-heat or thermal stream
Latin letters	
A	heat-transfer area, m^2
$c_{p,g}$	specific heat capacity of the equivalent external thermal stream, kJ/(kg·K)
C_{min}^{sch}	scheme-imposed minimum thermodynamic consumption, kJ/kg_{CA}
E	Claude–Heylandt expander mass-flow fraction, –
Ex	exergy, kJ
ex	specific exergy, kJ/kg
Ex_e^{tur}	physical exergy remaining in the turbine-exhaust stream, kJ/kg_{CA}
Ex_{LA}	exergy transferred internally by the stored liquid air, kJ/kg_{CA}
Ex_Q^{aux}	physical exergy rejected by the auxiliary refrigeration system, kJ/kg_{CA}
$Ex_{Q_{cp}}$	physical exergy rejected with compressor-cooling heat, kJ/kg_{CA}
Ex_{Q_f}	exergy of the useful liquefaction cooling product, kJ/kg_{CA}
$Ex_{Q_R}^{w}$	recoverable chilled-water cooling exergy, kJ/kg_{CA}
$Ex_{Q_e}^{tur}$	turbine-exhaust exergy credited as a recoverable cooling product, kJ/kg_{CA}
$Ex_{Q_i}^{WH}$	inlet physical-exergy contribution of the external thermal stream, kJ/kg_{CA}
$Ex_Q^{T_{11}}$	exergy supplied with heat during ideal isothermal expansion, kJ/kg_{CA}
ExRF	exergetic recovery factor, %
F_{dis}	total exergetic fuel of the discharge stage, kJ/kg_{CA}
f_{COP}	ratio COP_{real}/COP_C, –
h	specific enthalpy, kJ/kg
I	internal exergy destruction, kJ/kg_{CA}
L	exergy loss, kJ/kg_{CA}
$L_{Q_e}^{tur}$	unrecovered turbine-exhaust exergy loss, kJ/kg_{CA}
m_g	external-stream mass ratio, kg_g/kg_{CA}
p	pressure, MPa
P_{tot}	total multi-product exergy output, kJ/kg_{CA}
q_{aux}	specific cooling duty supplied by the auxiliary refrigeration system, kJ/kg_{CA}
q_f	specific cooling capacity of air, kJ/kg_{CA}
q_{iz}	heat penetration due to imperfect insulation, kJ/kg_{CA}
q_n	warm-end unrecovered cooling duty, kJ/kg_{CA}
Q	heat duty, kJ
R	specific gas constant, J/(kg·K)

RF	mechanical-energy recovery factor, %
s	specific entropy, kJ/(kg·K)
T	temperature, K
tur	turbine
T_m	mean thermodynamic temperature
T_{EV}^{aux}	evaporation temperature of the auxiliary refrigeration system, K; assumed equal to T_7 in the ideal auxiliary evaporator model
W	mechanical work kJ/kg_{CA}
w	specific mechanical work, kJ/kg_{CA}
w_0	net-specific liquefaction work, MJ/kg_{LA}
$w_{0,tur}$	recovered turbine work per kilogram of liquid air, MJ/kg_{LA}
y	fraction of liquefied air, kg_{LA}/kg_{CA}
Subscripts	
0	environment, in equilibrium with the environment
1, 2. . ., 12	thermodynamic state points
4′	saturated liquid state after throttling and separation
4″	saturated vapor state after throttling and separation
aux	auxiliary refrigeration system
C	Carnot reference
comp	compressor train
cp	compressor
e	outlet or exit
ex	exergetic
g	external thermal stream gas
i	inlet, summation index
iz	insulation
L	loss
LA	liquid air
m	mean
max	maximum
min	minimum
P	cryogenic pump
T	isothermal process
tur	turbine
u	useful
w	water
WH	waste heat
Superscripts	
M	mechanical exergy component
T	thermal exergy component or isothermal reference process, according to context
sch	scheme-imposed contribution
w	water
W	work-only performance indicator
WH	waste heat
$\delta Q = 0$	adiabatic process
Greek symbol	
Δh_T	enthalpy variation along an isothermal path, kJ/kg
ΔT_n	imposed warm-end terminal temperature difference in a recuperator, K
η	efficiency
$\eta_{cp,T}$	compressor isothermal efficiency
η_{ex}	structural liquefaction exergetic indicator
$\eta_{ex,global}$	multi-product global exergetic efficiency
$\eta_{ex,global}^{W}$	work-only global exergetic efficiency

Ψ	share of exergy destruction, exergy loss, or a scheme-imposed contribution
θ	exergetic factor of temperature

References

1. Koohi-Fayegh, S.; Rosen, M.A. A Review of Energy Storage Types, Applications and Recent Developments. *J. Energy Storage* **2020**, *27*, 101047. [CrossRef]
2. Frate, G.F.; Ferrari, L.; Desideri, U. Energy Storage for Grid-Scale Applications: Technology Review and Economic Feasibility Analysis. *Renew. Energy* **2021**, *163*, 1754–1772. [CrossRef]
3. Stanciu, C.; Stanciu, D.; Gheorghian, A.-T.; Tănase, E.-B.; Dobre, C.; Spiroiu, M. Maximum Exergetic Efficiency Operation of a Solar Powered H2O-LiBr Absorption Cooling System. *Entropy* **2017**, *19*, 676. [CrossRef]
4. Borri, E.; Tafone, A.; Romagnoli, A.; Comodi, G. A Review on Liquid Air Energy Storage: History, State of the Art and Recent Developments. *Renew. Sustain. Energy Rev.* **2021**, *137*, 110572. [CrossRef]
5. Vecchi, A.; Li, Y.; Ding, Y.; Mancarella, P.; Sciacovelli, A. Liquid Air Energy Storage (LAES): A Review on Technology State-of-the-Art, Integration Pathways and Future Perspectives. *Adv. Appl. Energy* **2021**, *3*, 100047. [CrossRef]
6. Qi, M.; Park, J.; Lee, I.; Moon, I. Liquid Air as an Emerging Energy Vector towards Carbon Neutrality: A Multi-Scale Systems Perspective. *Renew. Sustain. Energy Rev.* **2022**, *159*, 112201. [CrossRef]
7. She, X.; Wang, H.; Zhang, T.; Li, Y.; Zhao, X.; Ding, Y.; Wang, C. Liquid Air Energy Storage—A Critical Review. *Renew. Sustain. Energy Rev.* **2025**, *208*, 114986. [CrossRef]
8. Peng, X.; She, X.; Cong, L.; Zhang, T.; Li, C.; Li, Y.; Wang, L.; Tong, L.; Ding, Y. Thermodynamic Study on the Effect of Cold and Heat Recovery on Performance of Liquid Air Energy Storage. *Appl. Energy* **2018**, *221*, 86–99. [CrossRef]
9. Tafone, A.; Borri, E.; Comodi, G.; Van Den Broek, M.; Romagnoli, A. Liquid Air Energy Storage Performance Enhancement by Means of Organic Rankine Cycle and Absorption Chiller. *Appl. Energy* **2018**, *228*, 1810–1821. [CrossRef]
10. Vecchi, A.; Li, Y.; Mancarella, P.; Sciacovelli, A. Multi-Energy Liquid Air Energy Storage: A Novel Solution for Flexible Operation of Districts with Thermal Networks. *Energy Convers. Manag.* **2021**, *238*, 114161. [CrossRef]
11. Liu, Z.; Kim, D.; Gundersen, T. Optimal Recovery of Thermal Energy in Liquid Air Energy Storage. *Energy* **2022**, *240*, 122810. [CrossRef]
12. Peng, X.; She, X.; Li, C.; Luo, Y.; Zhang, T.; Li, Y.; Ding, Y. Liquid Air Energy Storage Flexibly Coupled with LNG Regasification for Improving Air Liquefaction. *Appl. Energy* **2019**, *250*, 1190–1201. [CrossRef]
13. Dzido, A.; Krawczyk, P.; Wołowicz, M.; Badyda, K. Comparison of Advanced Air Liquefaction Systems in Liquid Air Energy Storage Applications. *Renew. Energy* **2022**, *184*, 727–739. [CrossRef]
14. Kılıç, M.; Altun, A.F. Comprehensive Thermodynamic Performance Evaluation of Various Gas Liquefaction Cycles for Cryogenic Energy Storage. *Sustainability* **2023**, *15*, 16906. [CrossRef]
15. Urduza, D.C.; Grosu, L.; Gaiu, G.L.; Șerban, A.; Dobrovicescu, A. Energetic and Exergetic Analysis of the Cryogenic Air Liquefaction Plant Based on the Simple Linde-Hampson Cycle. In Proceedings of the Sixteenth International Conference on Thermal Engineering: Theory and Applications (ICTEA 2025), Bucharest, Romania, 18–20 June 2025; Volume 1.
16. Urduza, D.C.; Grosu, L.; Percembli (Chelmuș), A.A.; Șerban, A.; Dobrovicescu, A. Structural Optimization of Cryogenic Gas Liquefaction Based on Exergetic Principles—The Linde–Hampson Cycle. *Axioms* **2025**, *14*, 785. [CrossRef]
17. Urduza, D.-C.; Grosu, L.; Serban, A.; Percembli (Chelmuș), A.A.; Dobrovicescu, A. Optimization of Cryogenic Gas Separation Systems Based on Exergetic Analysis—The Claude–Heylandt Cycle for Oxygen Separation. *Entropy* **2026**, *28*, 125. [CrossRef] [PubMed]
18. Szablowski, L.; Krawczyk, P.; Wolowicz, M. Exergy Analysis of Adiabatic Liquid Air Energy Storage (A-LAES) System Based on Linde–Hampson Cycle. *Energies* **2021**, *14*, 945. [CrossRef]
19. Khoshgoftar Manesh, M.H.; Ghorbani, B. Energy and Exergy Analyses of an Innovative Energy Storage Configuration Using Liquid Air Integrated with Linde-Hampson Liquefaction System, Molten Carbonate Fuel Cell, and Organic Rankine Cycle. *J. Energy Storage* **2022**, *47*, 103676. [CrossRef]
20. Incer-Valverde, J.; Hamdy, S.; Morosuk, T.; Tsatsaronis, G. Improvement Perspectives of Cryogenics-Based Energy Storage. *Renew. Energy* **2021**, *169*, 629–640. [CrossRef]
21. Bucsa, S.; Serban, A.; Balan, M.C.; Ionita, C.; Nastase, G.; Dobre, C.; Dobrovicescu, A. Exergetic Analysis of a Cryogenic Air Separation Unit. *Entropy* **2022**, *24*, 272. [CrossRef] [PubMed]
22. Hamayun, M.H.; Ramzan, N.; Hussain, M.; Faheem, M. Evaluation of Two-Column Air Separation Processes Based on Exergy Analysis. *Energies* **2020**, *13*, 6361. [CrossRef]
23. Percembli (Chelmuș), A.A.; Dupuy, A.; Grosu, L.; Dima, D.; Dobrovicescu, A. Exergetic Analysis and Design of a Mechanical Compression Stage—Application for a Cryogenic Air Separation Plant. *Entropy* **2025**, *27*, 532. [CrossRef] [PubMed]
24. Klein, S.A. *Engineering Equation Solver*; 32-bit Professional V9.457-3D; F-Chart Software: Madison, WI, USA, 2013.

25. Lemmon, E.W.; Jacobsen, R.T.; Penoncello, S.G.; Friend, D.G. Thermodynamic Properties of Air and Mixtures of Nitrogen, Argon, and Oxygen From 60 to 2000 K at Pressures to 2000 MPa. *J. Phys. Chem. Ref. Data* **2000**, *29*, 331–385. [CrossRef]
26. Yang, M.; Feng, X.; Liu, G. Heat Exchanger Network Design Considering the Heat Pump Performance. *Chem. Eng. Trans.* **2014**, *39*, 1099–1104. [CrossRef]
27. Etoumia, A.; Jobson, M.; Emtir, M. Shortcut Model for Predicting Refrigeration Cycle Performance. *Chem. Eng. Trans.* **2015**, *45*, 217–222. [CrossRef]
28. Turek, V.; Kilkovský, B.; Daxner, J.; Babička Fialová, D.; Jegla, Z. Industrial Waste Heat Utilization in the European Union—An Engineering-Centric Review. *Energies* **2024**, *17*, 2084. [CrossRef]
29. Mokarram, N.H.; Yu, Z.; Imran, M. A Techno-Economic Survey on High- to Low-Temperature Waste Heat Recovery Cycles for UK Glass Sector. *Int. J. Green Energy* **2023**, *20*, 1384–1400. [CrossRef]
30. Guizzi, G.L.; Manno, M.; Tolomei, L.M.; Vitali, R.M. Thermodynamic Analysis of a Liquid Air Energy Storage System. *Energy* **2015**, *93*, 1639–1647. [CrossRef]
31. Kays, W.M.; London, A.L. Appendix B. In *Compact Heat Exchangers*; Krieger Pub Co.: Malabar, FL, USA, 1998; pp. 310–313. ISBN 978-1-57524-060-2.
32. Yilmaz, C. Thermodynamic Performance Analysis of Gas Liquefaction Cycles for Cryogenic Applications. *J. Therm. Eng.* **2018**, *5*, 62–75. [CrossRef]

Disclaimer/Publisher's Note: The statements, opinions and data contained in all publications are solely those of the individual author(s) and contributor(s) and not of MDPI and/or the editor(s). MDPI and/or the editor(s) disclaim responsibility for any injury to people or property resulting from any ideas, methods, instructions or products referred to in the content.